

Recent Trends in Charged Particle Optics and Surface Physics Instrumentation

Proceedings
of the 12th International Seminar,
held in Skalský dvůr near Brno, Czech Republic,
from May 31 to June 4, 2010,
organized by
the Institute of Scientific Instruments ASCR, v.v.i.,

Edited by Filip Mika

Published and distributed by the Institute of Scientific Instruments ASCR, v.v.i.,
technical editing by Miroslav Janáček, printed by MJ servis spol. s.r.o.

Copyright © 2010 by the Institute of Scientific Instruments ASCR, v.v.i. and individual contributors. All rights reserved. No part of this publication may be reproduced, stored in a retrieval system or transmitted in any form or by any means, electronic, mechanical, photocopying, recording or otherwise, without the written permission of the publisher, except as stated below. Single photocopies or single articles may be made for private study or research. Illustrations and short extracts from the text of individual contributions may be copied provided that the source is acknowledged, the permission of the authors is obtained and ISI ASCR, v.v.i. is notified.

The publishers have made every effort to reproduce the papers at their optimum contrast and with optimum resolution from materials provided by the authors. The publishers accept no liability for the loss of image quality resulting from supply of poor original material or improperly prepared digital records.

ISBN 978-80-254-6842-5

PREFACE

In the foreword before last in this for decades lasting series I expressed my doubts about continuation of the small, within the context of other scientific events a bit peculiar meeting of a relatively closed community. And in the previous preface I announced a change, namely change in the leading individual and consequently also probable change in the atmosphere perceived by participants. However, the last meeting passed smoothly and without surprises, two years elapsed in no time and the white sheet of paper calls for another preface.

Under what state of affairs at the host institute are we going to meet? There is one matter distinguishing this moment from the background of flying time. After several years of hectic negotiations, filling of forms and compiling piles of manifold paperwork, the so called "European money" from the structural funds started really to appear in this country. During whole this long time Czech scientists perceived the action as a unique historical opportunity to get money for modern instrumentation in amounts normally unthinkable, at least inside the Czech Academy of Sciences. ISI grasped the opportunity like the clappers and distributed its effort into multiple directions. Worth of mentioning is the story of striving for purchase of devices of the types corresponding to the topic of this Seminar. This means, instrumentation for the scanning electron microscopy and surface analysis. Since 2005 ISI has participated in drafting a large project of a consortium of Brno universities and institutes covering both life and materials sciences, sized to amount in Euro dynamically varying up and down and peaking at about three fourths of billion. Within this project ISI planned to acquire altogether six apparatuses for photoemission and Auger spectromicroscopy, high resolution and environmental SEM and also an analytical SEM with all existing attachments in order to equip the new pavilion of the Methodological laboratory of electron microscopy on the ISI premises. Nice dreams, certainly! Some time in 2006 an idea emerged to build a 3 MeV synchrotron in Brno as a large infrastructure serving to the whole region of Central Europe. Again, ISI was a member of the consortium consisting solely of the Academy institutes, and contributed significantly via two young colleagues who compiled the technical project inspired by the ALBA synchrotron being built that time near Barcelona. In the financial plan there was again nice amount of money reserved for off-beamline instrumentation, i.e. microscopes and microprobe. In 2007 the other two departments of ISI started to plan a large separate ISI project entitled Application Laboratories of Advanced Microtechnologies and Nanotechnologies and comprising nearly all research directions pursued at ISI except the electron microscopy. It seemed us exaggerated to hedge the microscopes for the third time. Attempt of a single small institute to be awarded own project of structural funds looked hopelessly from the very beginning. However, first was ceased the synchrotron. Academy of sciences did not feel strong enough to put the project through. A bit later, our own project astonishingly gained the required support and in response to it, institute was forced out of the consortium project with reference to the accumulated burden possibly beyond so small institute. Thus, ISI became happy awardee of a large project not containing any microscopic instrumentation. Fortunately enough, we have been able to modify our project in order to release funds sufficient to purchase a front end microscope with a complete set of attachments. I think you also know a few fairy tales about someone who wanted too much and finally received nothing, do not you? After all, our story finished a bit better.

Allow me to believe that this Skalsky dvur meeting will finish much better and will inspire all of us to continue the tradition even further.

Luděk Frank

CONTENTS

HIGH RESOLUTION ELECTRON MICROSCOPY VIA LOCALIZED FIELD-EMITTED ELECTRONS T. L. Kirk, L. G. De Pietro, H. Cabrera, T. Bähler, U. Maier, U. Ramsperger, and D. Pescia	7
ELECTRON-OPTICAL INVESTIGATIONS ON COLD CATHODE ELECTRON BEAM SOURCES FOR HIGH-RATE PVD P. Feinäugle, G. Mattausch and F.-H. Rögner	9
MODIFICATION OF THE SCHOTTKY FE ZrO/W ELECTRON EMITTER F. Matějka, M. Horáček, V. Kolařík and S. Král	13
MAPPING OF DOPANTS BY ELECTRON INJECTION M. Hovorka, I. Konvalina and L. Frank	15
ELECTROSTATIC HEXAPOLE CORRECTOR FOR REDUCTION OF SPHERICAL ABERRATION WITHIN MINIATURISED COLUMNS R. Janzen	17
FORMATION AND VISUALIZATION OF NANOSTRUCTURES WITH SEM/FIB J. Jiruše	19
ELECTRON OPTICAL PROPERTIES OF THE CATHODE LENS COMBINED WITH A FOCUSING MAGNETIC/IMMERSION-MAGNETIC LENS I. Konvalina, M. Hovorka and I. Müllerová	21
OPTICAL AND SCANNING ELECTRON MICROSCOPIES IN EXAMINATION OF ULTRATHIN FOILS I. Konvalina, M. Hovorka, T. Fořt and I. Müllerová	23
RECENT DEVELOPMENTS AND IMPROVEMENTS OF EOD PROGRAM B. Lencová	25
COMPARISON OF TECHNIQUES FOR DIFFRACTION GRATING TOPOGRAPHY ANALYSIS M. Matějka, A. Rek, F. Mika, T. Fořt, J. Matějková	29
SUPERCONDUCTIVE PROPERTY AND MICROSTRUCTURE OF MgB ₂ / Al COMPOSITE MATERIALS K. Matsuda, M. Mizutani, K. Nishimura, T. Kawabata, Y. Hishinuma, S. Aoyama, I. Müllerová, L. Frank and S. Ikeno	33
IMAGING OF DOPANTS UNDER PRESENCE OF SURFACE AD-LAYERS F. Mika, M. Hovorka and L. Frank	35

PROSPECTS OF THE SCANNING LOW ENERGY ELECTRON MICROSCOPY IN MATERIALS SCIENCE Š. Mikmeková, M. Hovorka, I. Konvalina, I. Müllerová and L. Frank	37
<hr/>	
IMPROVED ABERRATION CORRECTORS FOR THE CONVENTIONAL AND THE SCANNING TRANSMISSION ELECTRON MICROSCOPE H. Müller, M. Haider, P. Hartel, S. Uhlemann, and J. Zach	39
<hr/>	
TRANSMISSION MODE IN SCANNING LOW ENERGY ELECTRON MICROSCOPE I. Müllerová, M. Hovorka and L. Frank	41
<hr/>	
SIMULATION OF CURVED AXIS SYSTEMS, IMAGING ENERGY FILTERS, BEAM SEPARATORS AND ELECTRON MIRRORS E. Munro, J. Rouse, H. Liu and L. Wang	43
<hr/>	
IMPACT OF A BEAM LIMITING APERTURE ON COULOMB INTERACTION IN A LOW-VOLTAGE FOCUSED ION BEAM SYSTEM T. Ohnweiler, K. Marianowski, and E. Plies	47
<hr/>	
RAY TRACING, ABERRATION COEFFICIENTS AND INTENSITY DISTRIBUTION M. Oral	49
<hr/>	
MAPPING THE LOCAL DENSITY OF STATES ABOVE VACUUM LEVEL BY VERY LOW ENERGY ELECTRON REFLECTIVITY Z. Pokorná, L. Frank	53
<hr/>	
OPTIMIZATION OF THE COLLECTION EFFICIENCY OF SECONDARY IONS FOR SPATIALLY RESOLVED SIMS IN CROSSBEAM DEVICES D. Preikszas, M. Aliman, H. Mantz, A. Laue, A. Brockhaus and A. Glasmachers	55
<hr/>	
PROPERTIES OF Bi LMIS WITH ION CLUSTERS T. Radlička	57
<hr/>	
ENERGY SELECTIVE SECONDARY ELECTRON DETECTION A SOLUTION TO SITE SPECIFIC SEM DOPANT MAPPING C. Rodenburg, M. A. E. Jepson, E. G. T. Bosch, M. Dapor	59
<hr/>	
TRANSMISSION AND REFLECTION MICROSCOPY WITHOUT LENSES J. M. Rodenburg, A. M. Maiden and M. J. Humphry	61
<hr/>	
OUTLINE OF AN ABERRATION-CORRECTED LOW-VOLTAGE PHASE ELECTRON MICROSCOPE H. Rose	63
<hr/>	

NANOSTRUCTURE AND MORPHOLOGY OF WOOD CARBON OBSERVED
BY LOW VOLTAGE ELECTRON MICROSCOPY

K. Sato, T. J. Konno, K. Suzuki and T. Suzuki

65

DETERMINATION OF PROXIMITY EFFECT FORWARD SCATTERING RANGE
PARAMETER IN E-BEAM LITHOGRAPHY

M. Urbánek, V. Kolařík, S. Král and M. Dvořáková

67

IMAGING OF THERMAL TREATED THIN FILMS ON SILICON SUBSTRATE
IN THE SCANNING LOW ENERGY ELECTRON MICROSCOPE

J. Zobačová, Š. Mikmeková, J. Polčák and L. Frank

69

HIGH RESOLUTION ELECTRON MICROSCOPY VIA LOCALIZED FIELD-EMITTED ELECTRONS

T. L. Kirk¹, L. G. De Pietro^{1*}, H. Cabrera^{1,2}, T. Bähler¹, U. Maier², U. Ramsperger¹, and D. Pescia¹

¹ Eidgenössische Technische Hochschule Zürich (ETHZ), Laboratorium für Festkörperforschung, Wolfgang-Pauli-Strasse 16, 8093 Zürich, Switzerland

² Ferrovac GmbH, Thurgauerstrasse 72, 8050 Zürich, Switzerland

*e-mail: depietro@phys.ethz.ch

Low beam energies have been implemented in a simplified scanning electron microscopy (SEM) technique; where the electron source, remote in standard SEMs, is brought within tens of nanometers to the object. This method, known as “near field emission scanning electron microscopy” (NFESEM) [1-3], is capable of imaging conducting surfaces with nanometer-scale resolution using beam energies less than 60 eV. The terminology “near” refers to the locality of the field-emitted electron source; which is to distinguish itself from the “remote” field emission (FE) gun sources used in standard SEMs. Furthermore it is not an optical measurement such as in scanning near-field optical microscopy, where an image is generated from exciting and collecting light diffracted in the near-field regime.

The main aim of this instrument is the realization of some kind of surface topography image due to the exposure of a primary beam of electrons, as it is rastered along the sample surface. This will be achieved by two distinct (although related) experiments: measuring the FE current while scanning and detecting the secondary electrons (SE)s generated when the electron beam impinges on the surface. Here, the FE properties, in accordance with the tip-sample separation, will be emphasized, since the variations in SE yield are directly proportional to the impinging primary electron beam. As a direct result of the geometrical dependence of primary beam generation, the lateral resolution is enhanced with decreasing tip-sample separation [1, 3], see figure 1. Moreover, a direct correlation between the image contrast and the FE current, where the image is enhanced with increasing FE current, has been observed. In addition to the high resolution capabilities of NFESEM, complementary scanning tunnelling microscopy measurements can be performed in the same scanning, as can be observed in figure 2.

It has been demonstrated that the effective emission radius is a crucial parameter in the estimation of the NFESEM resolution capabilities [4]; therefore the resolution of the image can be used to confirm the sharpness of the emitter. C. Edgcombe has derived a correlation between the curvature of a Fowler-Nordheim (F-N) plot and a function describing a hemispherical barrier, as it is varied along emitter surface. Although this model was designed for a “hemisphere on a post” geometry, we have applied it to our F-N data generating a reasonable estimation of the emitter radius [2]. However, the deduced angular spread of the beam did not yield the same range as the experimentally determined beam width. This discrepancy is most-likely due to the spherical nature of the emitter in the theory, as the associated equipotential surfaces deviate slowly with the polar angle at small distances [5]. A non-spherical nanometric field emitter, which more accurately represents the angular spread, will be introduced.

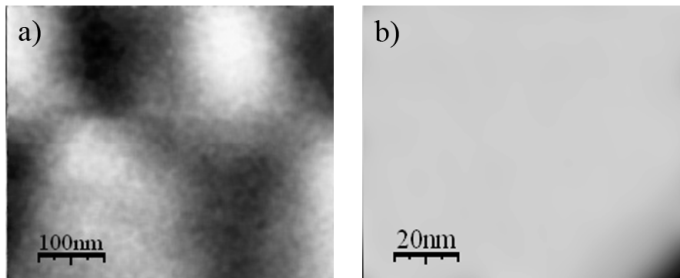


Figure 1: NFESEM image of gold grains on HOPG recorded at a tip-sample separation of (a) 100 nm and (b) 50 nm.

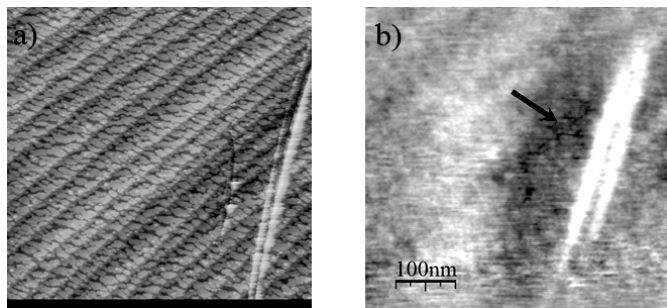


Figure 2: NFESEM micrographs (500 x 500 nm) of 1.1 MLs of Fe on a W (110) substrate, a) a subsequent STM micrograph ($I_T = 0.15$ nA and $V_B = 0.2$ V) ($I_{FE} = 20 - 50$ nA and $E_p = 40.7$ eV) and b) previous SE-NFESEM image recorded at 20 nm ($I_{FE} = 20 - 50$ nA and $E_p = 40.7$ eV). The arrow indicates the Fe islands.

References:

- [1] Kirk T. L., Ramsperger U., and Pescia D., J. Vac. Sci. Technol. B 27 (2009), p. 152-155.
- [2] Kirk T. L., Scholder O., De Pietro L. G., Ramsperger U., and Pescia D., Appl. Phys. Lett. 94 (2009), p. 153502(1)-153502(3).
- [3] Kirk T. L., Near Field Emission Scanning Electron Microscopy, Ph D thesis, Swiss Federal Institute of Technology, Zürich (2010).
- [4] Kirk T. L., De Pietro L. G., Ramsperger U., and Pescia D., Ultramicroscopy 109 (2009), p. 463-466.
- [5] Xanthakis J. P., Kyritsis A., Kokkorakis G. C., Scholder O., and Kirk T. L., unpublished.

ELECTRON-OPTICAL INVESTIGATIONS ON COLD CATHODE ELECTRON BEAM SOURCES FOR HIGH-RATE PVD

P. Feinäugle^{1*}, G. Mattausch¹ and F.-H. Rögner¹

¹ Fraunhofer Institute for Electron Beam and Plasma Technology – FEP
Winterbergstrasse 28, 01277, Dresden, Germany
*e-mail: peter.feinaeugle@fep.fraunhofer.de

Abstract

Electron Beams (EB) are known to be powerful and versatile tools for evaporation of various kinds of materials. At the other hand, conventional high-power electron beam sources based upon thermionic emitters are expensive and therefore in many thin film processes not applicable because of economic considerations. Electron beam sources with cold cathodes stimulated by high-voltage glow discharges (HVGD) have recently attracted enhanced interest at FEP mainly because of their prospects as economic beam sources for physical vapor deposition (PVD).

Particle-in-cell simulations (PIC) of the high-voltage glow discharge and of the beam formation in a simple geometry have been carried out to study the effects of the electrodes' geometry and of some discharge parameters on the electron-optical characteristics.

To create a powerful, cost efficient and low-maintenance EB evaporator system for industrial PVD processes, a thermally isolated ("hot") crucible with an integrated beam bending system and a specially shaped vapor aperture has been developed and tested together with a cold-cathode EB gun.

PIC Simulation of HVGD EB sources

Cold cathode beam sources have been investigated since long times [1], linked to applications as different as evaporation [3], EB welding [4], EB melting and refining [5] and pumping of lasers [6] to name just the most important.

Inside HVGD EB guns, a high-voltage glow discharge is sustained. The ion bombardment of the cathode delivers secondary electrons which are accelerated across the plasma sheaths and then form the beam (Fig.1). While in thermionic beam sources which operate under vacuum, the electric fields and electron paths conditions are mainly determined by the geometric arrangement of electrodes, in HVGD the space charge of different charged particles in the accelerating gap and the plasma contribute to particle dynamics as well and have to be taken into account in a simulation. The presence of plasma and of ion space charge layers is not reflected by standard electron ray tracing solvers. Therefore we tried to simulate the HVGD and beam forming in this environment with the particle-in-cell (PIC) plasma simulation program OOPIC Pro™ [6] which is based on the code XOPIC [7].

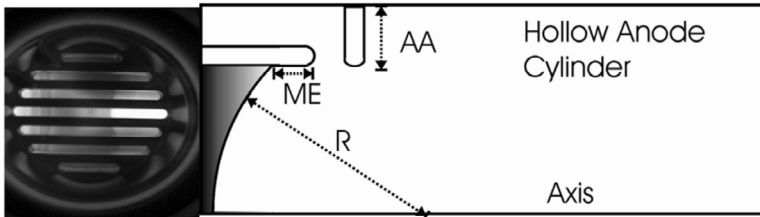


Fig. 1: View into the cathode compartment of a HVGD EB source, the cathode on top and anode plasma at the bottom. Photography on the left and schematic picture with the main geometrical parameters on the right.

In PIC codes, charged particles and plasmas are represented by “super-particles” with mass and charge of many (in our simulation: 10^6) physical particles [8]. The fields are calculated on a mesh and the particles dynamic behavior is determined using first principles. OOPIC Pro™ calculates two spatial and tree velocity components and considers collisions via a Monte Carlo algorithm.

A good consistence between the simulation results and experimental findings like global discharge parameters or plasma- and beam - properties could be found. But because these are mostly related to specific beam-sources, we would like to give a more general qualification of some main parameters and their influencing on the shape of the beam.

The main parts of the common electrode arrangement inside the cathode compartment of a HVGD gun are shown in Fig.1 (right). The geometry resembles a cylindrical hollow anode. An aperture ring connected to the (anodic) side wall (AA) is placed in front of the cathode at a distance smaller than the axial sheath width between cathode and plasma.

This anode is effectively focusing the ions towards the center of the cathode where a small borehole might let the beam pass off the discharge chamber [9]. For electron beams, Induni [10] placed this disk with small inner radius in front of the cathode. Focusing the ions has the advantage of smaller emission zones which on the other hand leads to enhanced sputtering. Generally, the cathode has a spherical shape with a certain radius of curvature (R) which serves as a focusing element. A cylindrical shielding electrode (ME) at the same potential supports this effect. The whole system resembles an electrostatic two-cylinder lens. Beside the already mentioned electrode parameters, the space charge density was varied as well. A statistical scheme similar to the one used by Felba [11] for optimization of real guns has been employed for setting up our computer experiments. As an example, the influence of the space charge density on the beam is shown in Fig.2 (left). Some statistical results are displayed in Fig.2 (right). The correlations give the relative effects of the four parameters on the axial position of the crossover in strength and direction, irrespective of the influence of the other parameters.

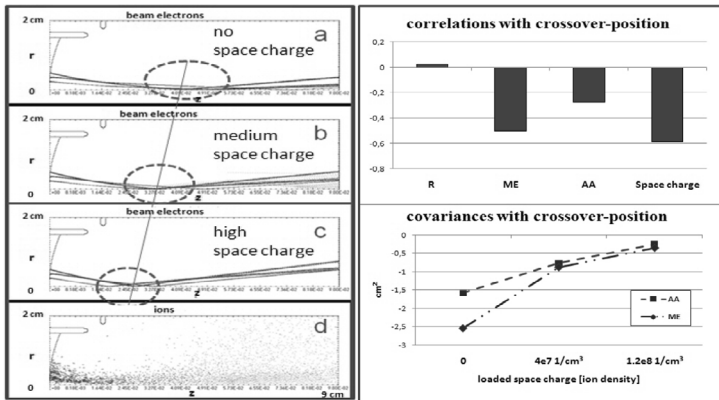


Fig. 2: Left (a-c): Effect of growing plasma and sheath space charge on the beam formation represented by three beamlets emitted from cathode segments: the cross-over position (circles) moves closer to the cathode. (d): ion distribution for the case (c)
Right: Relative effects of the investigated parameters on axial crossover position (top), absolute influence of relative space charge density on the effects of electrodes ME and AA (bottom).

The strongest effects could be achieved with elongation of the shielding electrode (ME) and a growing space charge, both acting converging. The third graph in Fig.4 shows that the presence of space charge diminishes the influence of the electrodes' shape on the field and therefore on beam formation. It also appeared to have a stabilizing effect on beam quality despite that the beamlets starting from different cathode segments were influenced rather nonlinearly. The principal feasibility of modeling a HVGD and the relevant beam forming mechanisms therein employing the commonly used PIC software OOPIC could be demonstrated.

High-efficient crucible for copper PVD

Beside to the EB gun, there is a remarkable potential for technological improvements of PVD processes in vacuum. The development of a new crucible was intended to cope with three different problems: the need of complicated magnetic coils and their supplies for beam bending, the weak material efficiency of many evaporation systems and the need for feeding devices in long running systems in the industrial production. As major features, it incorporates a thermally isolated graphite crucible, a shaped vapor aperture and an integrated beam bending system. The new crucible was tested in the high-rate deposition of copper onto 3D plastic parts to produce metallic EMI shielding layers for electronic devices as mobile phones or laptops. The available ingot volume allows for continuous production over several days without material feeding, venting or cooling down. The thermal isolation around the graphite block is contained in a water-cooled case.

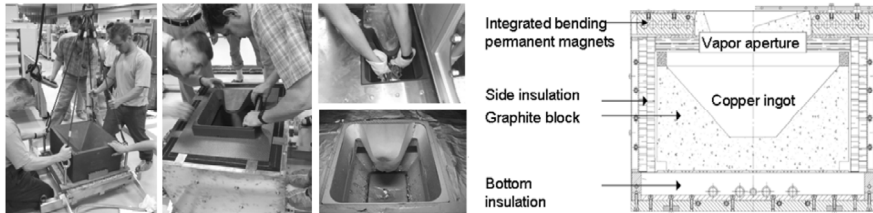


Fig. 3: Assembly and layout of the thermally isolated graphite crucible.
(From left to right: graphite block, vapor aperture, filling with copper pieces, almost consumed molten copper ingot, cross section.)

This helps improving the beam power utilization and reduces the thermal load to the substrate as well as to the vacuum chamber at the same time. The shaped vapor aperture cut into the cover plate lets pass those vapor particles which are directed towards the substrate but holds back those parts of the vapor flux which would otherwise hit the chamber wall. To direct the electron beam towards the evaporation site, the crucible unit is equipped with an integrated beam bending system made of permanent magnets. The magnetic field is generated in the vicinity of the ingot. By this design, it can simultaneously act as trapping field for backscattered electrons what is essential for preventing substrate damage in plastics' coating. The fields generated by different assemblies of permanent magnets were simulated with the numerical software suite "MAXWELL" and experimentally tested. When working in a single-point evaporator mode – which allows operation even without a fast dynamic beam deflection system – the rectangular opening can be partially covered with a tongue-shaped shield. Then, changing the position of the beam spot on the ingot surface allows for tuning the thickness distribution to create a flat layer profile on wide substrates at further reduced thermal load.

References

- [1] Dugdale R. A., Glow Discharge Materials Processing. Mills & Boon, London (1971); Новиков А.А., Источники электронов высоковольтного тлеющего разряда с анодной плазмой. Энергатомиздат, Москва (1983)
- [2] Denbnovetsky S. V., Melnyk V. G., Melnyk I. V., IEEE Transactions on Plasma Science **31** (2003), 987-993
- [3] Holliday J. H., Ketteringham T. A., GEC J. of Sc. & Techn. **44** (1978), 105-109
- [4] Chernov V. Proc.of the Conference on EB melting & refining, Reno, (1994), 259-268
- [5] Rocca J.J., Mayer J.D., Yu Z., Farell M., Applied Physics Letters **41** (1982), 811-813
- [6] http://www.txcorp.com/products/OOPIC_Pro/
- [7] Verboncoeur J.P., Langdon A.B., Gladd N.T., Comp. Phys. Comm. **87** (1995), 199-211
- [8] Birdsall C.K., Langdon A.B., McGraw Hill Book; New York (1985)
- [9] Hailer C., Naturwissenschaften **26** (1938), 382
- [10] Induni G., Helv. Phys. Acta **20** (1947), 463
- [11] Felba J., Vacuum **55** (1999), 223-233

MODIFICATION OF THE SCHOTTKY FE ZrO/W ELECTRON EMITTER

F. Matějka¹, M. Horáček^{1*}, V. Kolařík¹ and S. Král¹

¹ Institute of Scientific Instruments AS CR, Department of Electron Optics,
Královopolská 147, 61264 Brno, Czech Republic

*e-mail: mih@isibrno.cz

A Schottky electron emitter with a layer of ZrO_x [1,2] is used in our e-beam writing system working with a rectangular-shaped electron beam [3]. The low radius of the tip less than 300 nm is necessary for the proper function of the electron-optical system based on the principle of point projection [4].

We studied the influence of both the surface treatment and the change of the shape of the tip on the emission characteristics. We used the RIE (reactive ion etching) process for the tip radius modification, for regeneration of the active surface of the tip and repair of the incorrectly made tips. A radio frequency (13,56 MHz) RIE in barrel type reactor at 1000-2000 Pa and 200 W with gaseous mix of CF₄ and 16vol% O₂ were applied. The rate of the etching was only a few nm/minute at the starting room temperature. The SEM images of the cathode before and after RIE taken in JEOL JSM 6700F are shown in Fig. 1.

The influence of the RIE process on the emission characteristic was studied in an apparatus which allows cathode activation, debugging, testing and observation. The original electron gun of our e-beam writing system with emitter was attached in the apparatus. The standard cathode-extractor distance is 3 mm and the extractor voltage is also the working voltage of the e-beam writing system column. The apparatus consists of emitter (cathode), suppressor, extractor (anode), anode aperture and metallized scintillator. The measurement of a beam current from electrons bombarding scintillator is possible using external picoammeter. The apparatus is equipped with two inspection glasses for visual process monitoring. The first one is positioned on the optical axis of the apparatus behind the scintillator and it allows the observation of the cathode emission pattern. The second one is positioned radially and it allows the observation of the space between the suppressor and the anode.

In order to evaluate the influence of the RIE treatment on the emitter tip, the voltage/current characteristics were measured and simultaneously the emission pattern images projected on the scintillator were recorded by a camera. The following conditions were kept for all measurements: the cathode-extractor distance 3 mm, cathode heating current 1,5 A (approx. 1500 K) and suppressor bias 100 V. The comparison of the voltage/current characteristics of the tip is in Fig. 2. The comparison of the emission pattern images gives Fig. 3 [5].

References:

- [1] M. J. Fransen, M. H. F. Overwijk, P. Kruit, *Appl. Surf. Sci.* 146 (1999) 357.
- [2] B. Cook et al., *Ultramicroscopy* 109 (2009) 403.
- [3] A. Delong, V. Kolařík, *J. Phys. E: Sci. Instrum.*, 22 (1989) 612.
- [4] A. Delong et al., *10th ICEM*, Hamburg (1982) 455.
- [5] This research was supported by GA ASCR, grant no. IAA100650803, by MIT CR (TIP project No. FRTI1/576) and by EC and MEYS CR (project No. CZ.1.05/2.1.00/01.0017).

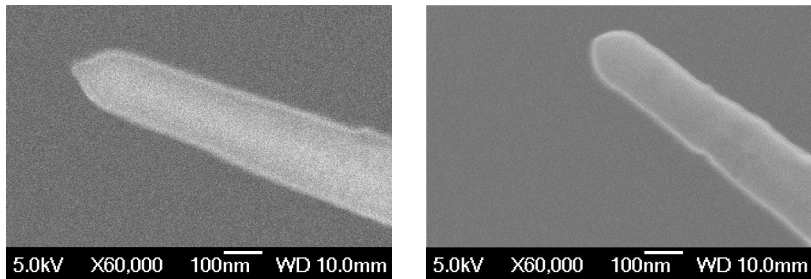


Fig. 1: SEM pictures of the emitter tip: before (left) and after (right) the RIE process.

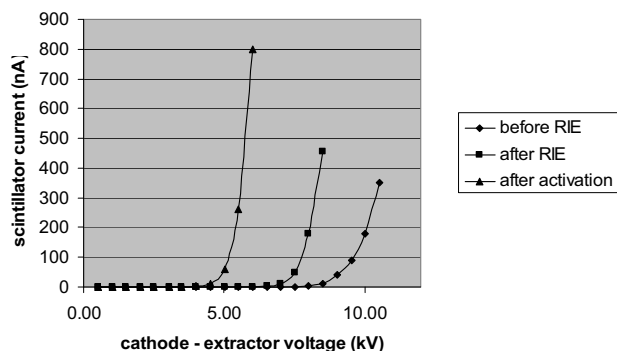


Fig. 2: Scintillator current versus cathode-extractor voltage for the emitter: before RIE, after RIE and after both the RIE process and the oxygen activation.

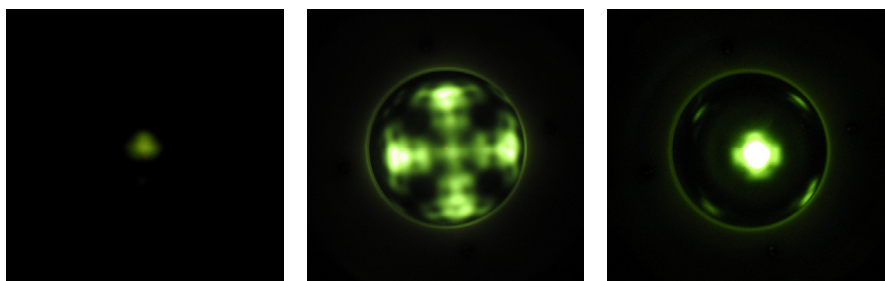


Fig. 3: The scintillator images of the emission pattern from the emitter: before RIE (left), after RIE (center) and after RIE and oxygen activation (right). Cathode-extractor voltage 8 kV, angular current density 4,5 :A/sr (left) and 51 :A/sr (right).

MAPPING OF DOPANTS BY ELECTRON INJECTION

M. Hovorka*, I. Konvalina and L. Frank

Institute of Scientific Instruments of the ASCR, v.v.i., CZ-612 64 Brno, Czech Republic

*e-mail: hovorka@isibrno.cz

Dopants in silicon structures locally modify the secondary electron emission, revealing in this way their distribution over the sample. Primary electron beam with energy around 1 keV is usually used for probing the doped structures. However, very low landing energy range has proved itself an efficient tool for mapping dopants in semiconductors [1, 2].

The cathode lens in an UHV SLEEM enables us to vary the electron landing energy in a broad range. Fig. 1a illustrates the contrast evolution between p-type patterns and n-type substrate as a function of landing energy. The dopant concentration in the p-type patterns ranges from 1.1×10^{16} to $1.1 \times 10^{19} \text{ cm}^{-3}$ (P16 to P19) while in the n-type substrate it amounts to $1.2 \times 10^{15} \text{ cm}^{-3}$ (N15). At around 5 keV the detected signal is dominated by backscattered electrons (BSE) so only negligible dopant contrast corresponds to the tiny relative dopant concentration not capable of altering the BSE yield. Decreasing the landing energy and diminishing the interaction volume brings an increase in the secondary electron yield. Consequently the detected signal is dominated by secondary electrons and a distinct contrast appears (see the 1 keV micrograph). Then the contrast weakens (118 eV frame) and becomes dependent on the dopant type and surface status. For n-type patterns on a p-type substrate the surface oxide plays an important role. At few eV the contrast was found influenced by the size of patterns (stripes of $25 \times 2000 \mu\text{m}$ in size in Fig. 1a vs. squares of sides 40, 20, and 5 μm in Fig. 1b), the electron dose (Fig. 1c), position of the patterns inside the field of view and the sample tilt.

The sample is a part of the cathode lens with electrostatic field between the sample and detector (YAG scintillator). The primary beam is scanned across the field of view by rocking so the impact angle of electrons on the surface sensitively depends on distance from the optical axis. In vicinity of a charged area on the surface the trajectories of electrons landing at low energy are significantly modified. We have simulated the electron trajectories within the cathode lens [3] when areas negatively biased with respect to the n-type substrate are scanned (Fig. 2). These areas represented the p-type patterns charged owing to the electron injection.

In Fig. 2a the potential difference of -1V was applied between the squares of sides 40, 20, 5 μm and the substrate, and electrons landed at 0.5 eV. The light gray color indicates total reflection of electrons on the YAG scintilllator, black color means reflection of electrons into the detector bore, and the gray area of the sample is where electrons impact on its surface. In Fig. 2b and 2c the landing energy was changed to 1.1 eV and in Fig. 2c the squares were moved 100 μm off the optical axis. Obviously the bright rims (see Fig. 1b, frames for 5 eV and 2 eV, and Fig. 1c) are caused by reflection of the primary beam on the scintilllator. When slightly increasing the simulated landing energy (1.3 eV in Fig. 2b) the bright rims and black areas suddenly disappear, which does not fit the experiment. However, the simulation model disregards e.g. the energy spread of the primary beam and any local surface tilts. The surface tilt significantly modifies the lateral component of the cathode lens field, which deflects electron trajectories. [4]

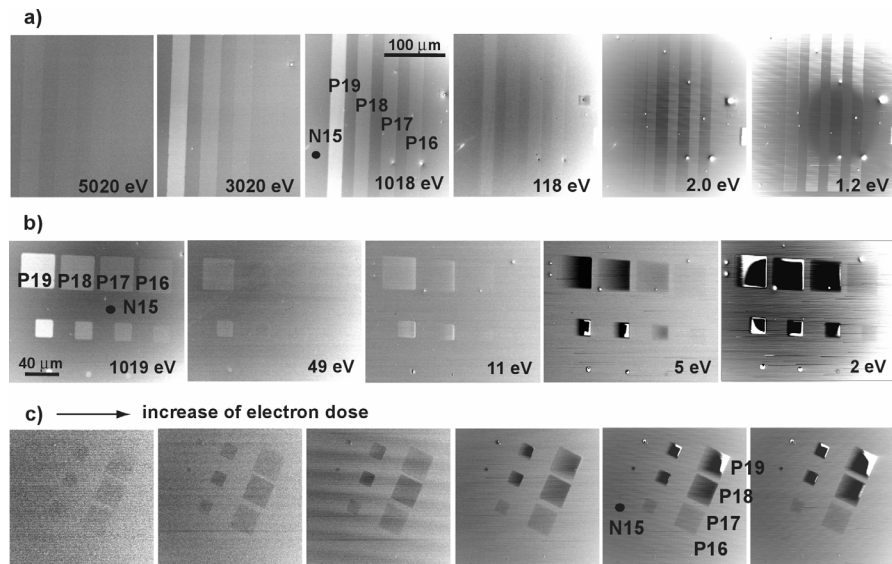


Figure 1 P-type patterns (Px) of dopant concentrations x on a n-type substrate (N15): contrast evolution as a function of the electron landing energy, the size of patterns (a, b) and the electron dose injected (c, landing energy 2.3 eV).

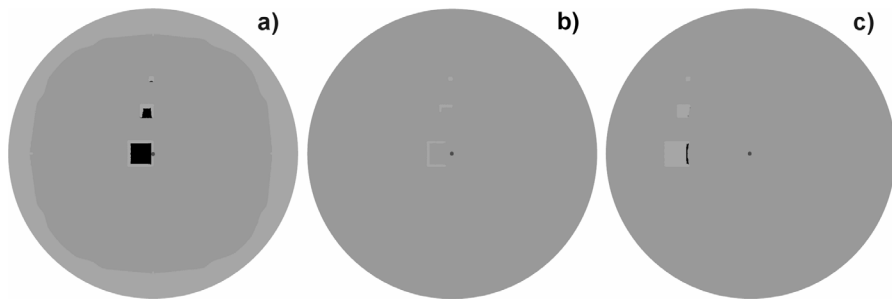


Figure 2 Behavior of electrons for the squares negatively biased with respect to the substrate: light gray area: total reflection on the YAG scintillator, black area: total reflection into the detector bore, gray area: impact on the sample. Potential difference between squares and substrate -1V, electron landing energy (a) 0.5eV, (b) 1.1eV, (c) 1.1eV; (c) squares moved 100 μm off the optical axis. Dark point indicates the centre of the field of view.

References:

- [1] Frank L., Müllerová I., Ultramicroscopy 106 (2005), p. 28-36.
- [2] Hovorka et al., Proceedings of 6th International Workshop on Leem/Peem (2006), Trieste, p. 110.
- [3] Dahl D. A., Int. J. Mass Spectrom. 200 (2000), p. 3-25.
- [4] Supported by the GACR project no. GP102/09/P543 and by the GAASCR project no. IAA100650803.

ELECTROSTATIC HEXAPOLE CORRECTOR FOR REDUCTION OF SPHERICAL ABERRATION WITHIN MINIATURISED COLUMNS

R. Janzen¹

¹ Laboratorium für Elektronenmikroskopie, Karlsruher Institut für Technologie (KIT), Engesserstr. 7, D-76131 Karlsruhe, Germany

* e-mail: info@dr-janzen.de

Charged particle optics is a continuously developing and expanding technology with a meanwhile broad area of application. But wherever you look aberrations, especially the spherical aberration, are omnipresent. In the highly sophisticated area of electron microscopy correctors are meanwhile commonly used. Hexapole correctors are state of the art and are continuously advanced by the famous experts at CEOS company in Germany.

Nowadays charged particle optics finds its way into miniaturized applications. Whereas miniaturised columns including mini lenses exist, the commonly used correctors are too complex for a use in miniaturised single or multicolumn systems. Nevertheless the general principle of hexapole correctors may be transferred to such systems.

Accepting the disadvantage that the chromatic aberration is clearly worsened a purely electrostatic design opens the door to miniaturisation and integrated fabrication.

The key is the fact that a hole with threefold shape within an aperture separating two electric fields with different strengths produces a superposition of a round lens field and a hexapole field. In simple terms all that has to be done in order to use such hexapole fields for reduction of spherical aberration is to pile up and (voltage-)supply apertures with threefold shaped holes in a sophisticated way. The coupling of the round lens- and the hexapole fields as well as the coupling of the field strengths with distances and voltages of the apertures and therefore velocity changes complicate the labyrinth where to find the way of realizing the generalised principle of a hexapole corrector. Let's just remind the latter:

- Two identical hexapoles and round lenses are arranged that way that the midplane of the first hexapole is imaged into the midplane of the second one.
- The field ray has a zero in the midplanes of both hexapoles and therefore keeps its rotationally symmetry.
- The intermediate image plane becomes a symmetry plane of the field ray and the entire assembly.

The design depicted in figure 1 shows an example of such an assembly. In order to generate it, a computer simulation procedure based on the charge simulation method was used.

Some details: The voltages of the apertures were adjusted successively by calculating a field ray through the assembly via ray tracing. Finally bundles of axial rays with varying initial angles (and energies) were calculated through the completely adjusted assembly. The threefold astigmatism, the chromatic and the spherical aberration were deduced out of the course of the rays of the bundle by mathematical analysis.

Results: The hexapole strengths of single apertures having holes with a threefold shape, denoted by hexapole apertures in the following, showed to be insufficiently small. Building up a corrector yielding negative values of C_s succeeded by using duplets of hexapole apertures.

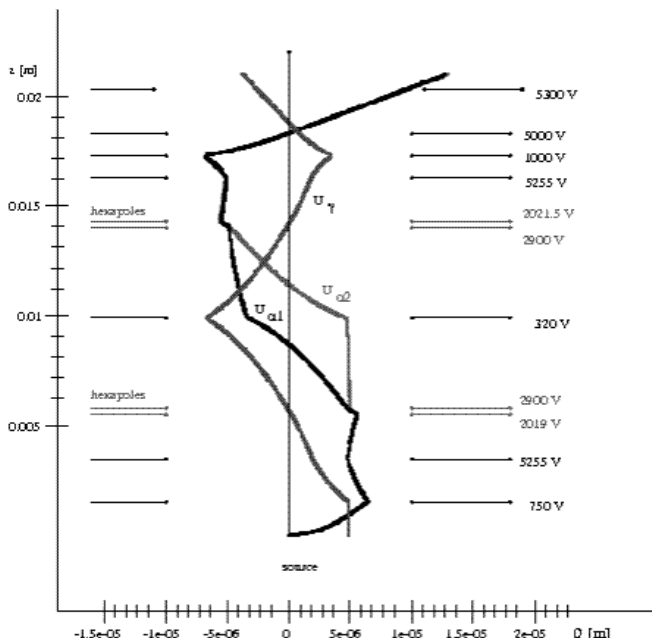


Figure 1: Positions and optimum voltages of the apertures and course of the fundamental rays within an example system of the electrostatic C_s -mini corrector. $U_{\alpha 1}$ and $U_{\alpha 2}$ differ in the area between the hexapole apertures because the azimuth of their starting angle differs by 60 degrees.

Outlook: In order to reduce the chromatic aberration of the C_s -mini corrector the minimum voltages must be increased without losing hexapole strength. Using triplets of hexapole apertures (in analogy to electrostatic round lenses) instead of duplets seems to be a promising strategy.

All in all the new design of an electrostatic C_s -mini corrector is a promising concept for reducing or correcting spherical aberrations in miniaturised single or multi column systems with highly monochromatic beamlets.

Acknowledgement

Last but not least I want to express my special thanks to ICT GmbH, Ammerthalstr. 20, 85551 Heimstetten, Germany for financing the entire project.

FORMATION AND VIZUALIZATION OF NANOSTRUCTURES WITH SEM/FIB

J. Jiruš*

Tescan a.s., Libušina třída 21 623 00, Brno Czech Republic

*e-mail: jaroslav.jiruse@tescan.cz

Focused ion beam (FIB) in combination with scanning electron microscopy (SEM) enables fabrication and analysis of structures on a scale of a few tens of nanometers. Besides micro- and nanomachining of a specimen surface by metal deposition and milling, the technique can find its use also in ion beam lithography, implantation and material testing. Nanostructures created by FIB can be applied in many areas of research, like spintronics and plasmonics.

Spintronics, also known as magnetoelectronics, uses the spin of electrons in addition to their charge and is very promising in the field of technology, like sensorics (spin valve), non-volatile high-density data storage (vortex structures, racetrack memory) and magnetic-logic circuits. Spintronic structures are usually prepared by sputter deposition of layered structures, consisting of magnetic and non-magnetic metallic (or dielectric) thin films with the thickness ranging from 5 to 50 nm. Such nanostructures can be then used for examination of domain wall motion, spin-transfer-torque studies, magnetization dynamics, magnetic vortices, and others [1].

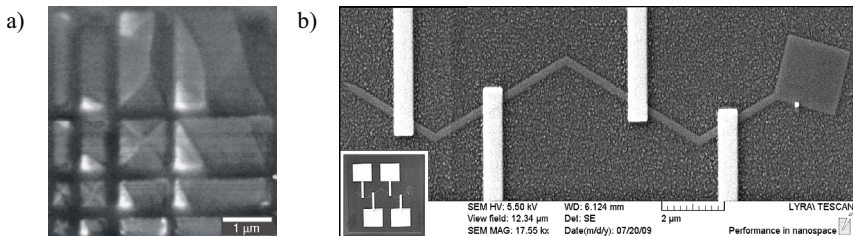


Fig. 1: An example of spintronic structures prepared by FIB. a) An image of magnetic domains in rectangular structures (vortices) fabricated by FIB and measured using magnetic force microscopy (MFM), b) Spin-valve nanowire (diameter: 200 nm, length: 16 μm) with Pt contacts formed by FIB deposition.

Plasmonics is an area of science that exploits the excitation and propagation of the surface plasmon polaritons (SPP) along the metal surface or metal/dielectric interface. Utilization of nanostructures appears to be a promising way to bypass optical diffraction limits in small photonic systems and to be used in a variety of applications. Therefore, formation of grooves into thin metallic films (e.g. Au, Ag, Pt, Al) is required in order to couple and decouple plasmons propagating along metal-dielectric interfaces and to fabricate various metallic micro- and nanostructures for generation of localized surface plasmons. The electromagnetic field in the vicinity of nanostructures can be enhanced by several orders of magnitude as a result of meeting resonance conditions for oscillating conduction electrons. This phenomenon

occurs especially in the resonant plasmonic antennas which can be used both for sensing (e.g. local spectroscopy of nanostructures) and radiation purposes (localized light sources for nanophotoelectronics).

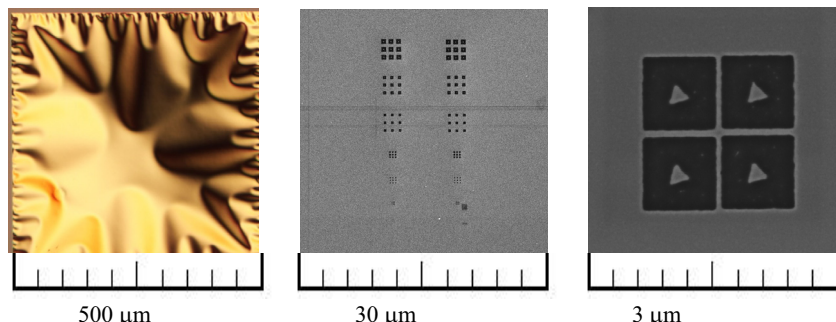


Fig. 2: Optical gold antennas prepared by etching of 20 nm thick Au layer on 30 nm thick silicon nitride membranes using FIB (Lyra-FEG Tescan).

The performance of modern FIB setups allows to mill the nanostructures with the ultimate milling resolution of approximately 10 nm at a reasonable speed. Tescan's LYRA, favorable combination of FIB and high resolution SEM, proved to be a valuable tool for preparation of nanostructures for applications in both spintronics and plasmonics. Together with Gas Injection System (GIS), milling and deposition steps can be easily performed without multi-step mask-based technological processes typical for electron beam lithography. Therefore, LYRA represents state-of-the-art technology designed for the most demanding users in the field of nanoscience. Further details about LYRA are available at www.tescan.com.

Acknowledgement:

The research has been carried out at Institute of Physical Engineering, Faculty of Mechanical engineering, Brno University of Technology under supervision of prof. T. Šikola. Nanostructures for spintronics were prepared in the scope of research project MŠMT 2E08017 by M. Urbánek. Nanostructures for plasmonics were prepared in the scope of research projects MSM0021630508, 2E08017 and LC06040 by O. Tomanec.

References:

- [1] Urbánek M., Uhliř V., Bábor P., Kolíbalová E., Hrnčíř T., Spousta J., and Šikola T., Proceedings of the FSI Junior Conference (2010), Brno.

ELECTRON OPTICAL PROPERTIES OF THE CATHODE LENS COMBINED WITH A FOCUSING MAGNETIC/IMMERSION-MAGNETIC LENS

I. Konvalina*, M. Hovorka and I. Müllerová

Institute of Scientific Instruments of the ASCR, v.v.i., Královopolská 147, 612 64, Brno,
Czech Republic

* e-mail: konvalina@isibrno.cz

Cathode lens (CL) is an electron optical element commonly used in the photo-emission electron microscopy (PEEM), low energy electron microscopy (LEEM) and last but not least in the scanning electron microscopy (SEM) [1]. Lenc and Müllerová [2,3] studied the basic optical parameters of the CL alone as well as in combination with a magnetic focusing lens, and derived approximate analytical expressions for the axial aberration coefficients for both cases. For the combination of lenses, the sequential arrangement of electrostatic and magnetic fields was considered. Several authors have claimed the aberration coefficients smaller for overlapped fields of the lenses under combination [4,5].

We have used the EOD software [6] for calculation of aberration coefficients for the sequential and overlapped fields. The simulated arrangement of the objective lens (OL) and specimen (cathode of the CL), showing also the axial magnetic field of the focusing and focusing immersion lenses, is in Figure 1. The spherical and chromatic aberration coefficients of the image side were calculated for the landing energy E_L varying from 10 keV to only 1 eV with the primary beam energy of $E_p = 10$ keV (see Table 1).

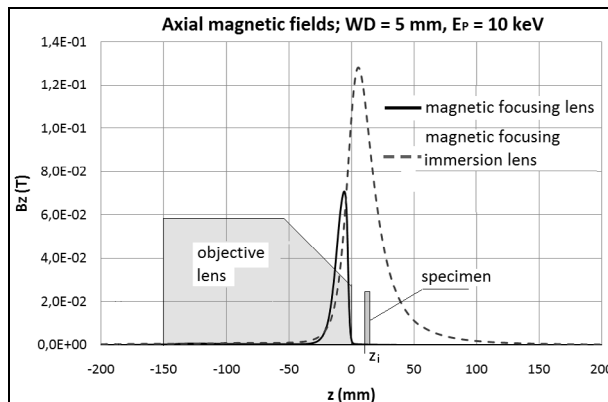


Figure 1 Simulated arrangement and axial magnetic fields of both objective lenses; $z_o = -10$ m (object plane), $z_i = WD = 5$ mm (image plane = working distance).

The spot size (see Figure 2) is calculated for a specific arrangement (object and image planes, optimum angular aperture for achieving the ultimate resolution, primary beam energy, geometry of objective lenses, cathode lens). The diffraction effect, spherical and chromatic aberrations are taken into account via convolution of confusion discs described by Gaussian functions (d_G) and defining the disc sizes by a diameter encircling some current fraction [7] (d_{BK}). As regards the image resolution, the simulations show that thanks to properties of the immersion magnetic lens the overlapped arrangement of the magnetic and electrostatic fields

is better for all landing energies. For lower landing energies the behaviour is dominated by influence of the cathode lens alone. [8]

E_L (eV)	Sequential field		Overlapped field	
	C_s (mm)	C_c (mm)	C_s (mm)	C_c (mm)
10000	30,716	11,535	3,0005	4,5955
5000	19,629	5,4875	1,8961	2,1381
1000	3,9984	0,80874	0,51174	0,36158
500	1,7521	0,34857	0,25414	0,17386
100	0,22091	0,051913	0,04488	0,033504
50	0,087664	0,023579	0,021072	0,016654
10	0,010039	0,0040207	0,0036703	0,0032824
5	0,003915	0,0019267	0,0017188	0,0016296
1	0,00048798	0,00039541	0,00031661	0,00034391

Table 1 The spherical and chromatic aberration coefficients of the image side for the systems of the sequential and overlapped fields.

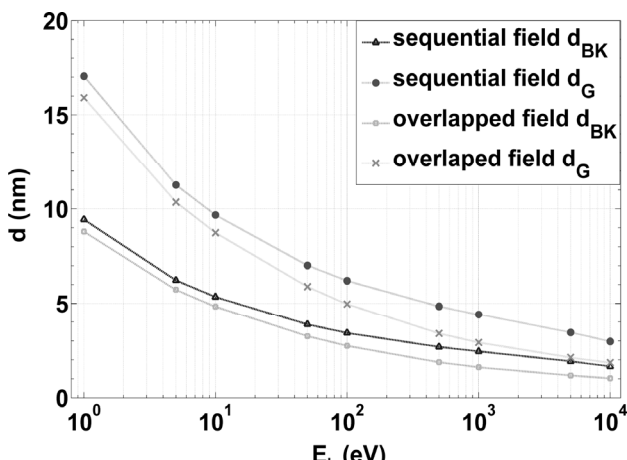


Figure 2 Spot size produced by two objective lenses as a function of the landing energy.

References:

- [1] Müllerová I., Frank L., Advances in imaging and electron physics **128** (2003), p. 309-443.
- [2] Lenc M., Müllerová I., Ultramicroscopy **41** (1992), p. 411-417.
- [3] Lenc M., Müllerová I., Ultramicroscopy **45** (1992), p. 159-162.
- [4] Khursheed A., Optik **113** (2002), p. 67-77.
- [5] Mankos M., Adler D., Veneklasen L., Munro E., Surface Science **601** (2007), p. 4733-4741.
- [6] Lencová B., Zlámal J., Microscopy and Microanalysis **13** (2007), p. 2-3.
- [7] Barth J.E., Kruit P., Optik **101** (1996), p. 101-109.
- [8] Supported by GAASCR under no. IAA100650902.

OPTICAL AND SCANNING ELECTRON MICROSCOPIES IN EXAMINATION OF ULTRATHIN FOILS

I. Konvalina*, M. Hovorka, T. Fořt and I. Müllerová

Institute of Scientific Instruments of the ASCR, v.v.i., Královopolská 147, 612 64, Brno,
Czech Republic

* e-mail: konvalina@isibrno.cz

Very low energy scanning transmission electron microscopy [1] is emerging as a novel tool for examination of ultrathin foils to learn more about the electron structure of solids. The electron micrographs provide image contrasts governed by the “effective thickness” of the sample proportional to the inner potential and at lowest energies the local density of electron states in the direction of impact of the electron wave starts to dominate. The optical methods are used during the sample preparation. The laser confocal microscope Olympus Lext OLS 3100 was used for preliminary observations of the 3 nm C foil prepared by magnetron sputtering in nitrogen atmosphere on a flat glass covered by a disaccharide layer. Disaccharide was dissolved in distilled water, dropped on glass, dried, covered with carbon and the foil was unstuck on a 25 µm period copper grid usually used for the transmission electron microscopy. The thickness was first estimated from the measurement by X-ray diffraction. Presented Figures show the layer flake imaged by the laser microscope and by low energy electrons in the reflected and transmitted mode. Similar experiments have been performed on a 3 nm Au foil [2].

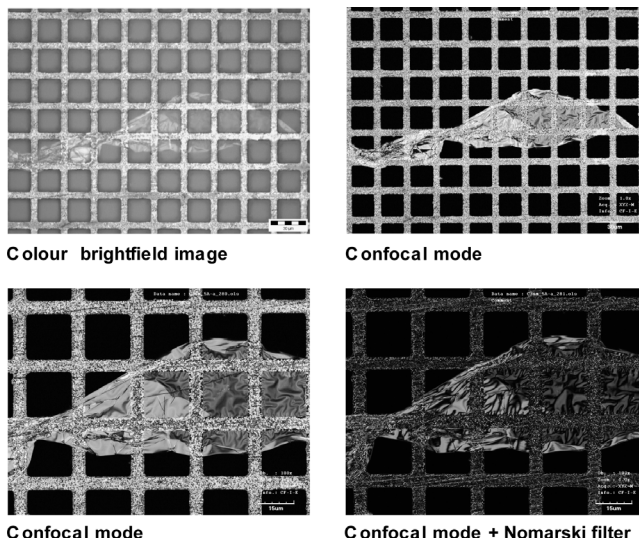


Figure 1 3 nm C foil imaged by the confocal microscope in different modes.

Images obtained by the laser confocal microscope show the layer in detail. Overlapping layers have different image contrast and even the structure of the layer is visible. Very low energy

scanning electron microscope is a capable tool for examination of ultrathin foils. At landing energy of about 1000 eV (reflected mode) the layers of the foil are clearly visible. Varying landing energies allow to distinguish different thickness of the layers. A strong contrast between the overlapping layers is visible at the landing energy of about 3000 eV (transmitted mode). The interaction volume is smaller with the decreasing landing energy, the structure of the layer becomes notable (see Figure 3 for $E_L = 500$ eV).

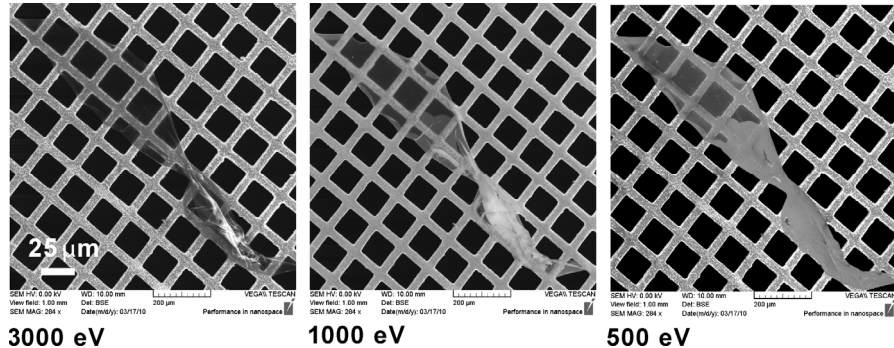


Figure 2 3 nm C foil imaged by UHV scanning low energy electron microscope – reflected mode. Primary beam energy $E_p = 6$ keV, landing energies of electrons $E_L = 3000$ eV, 1000 eV, 500 eV, working distance WD = 9 mm, primary current $I_p = 150$ pA.

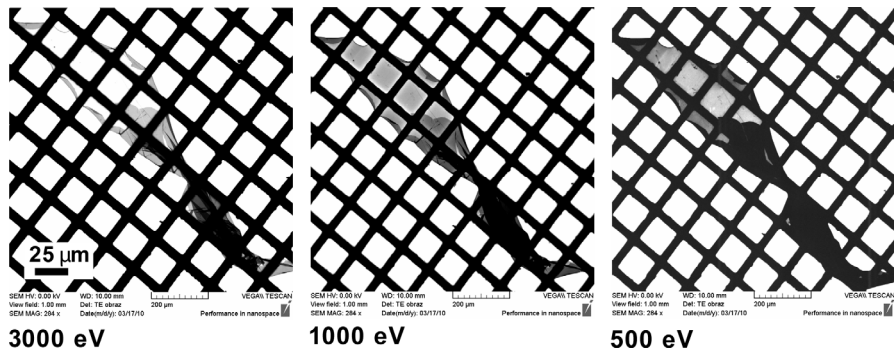


Figure 3 3 nm C foil imaged by UHV scanning low energy electron microscope – transmitted mode. Primary beam energy $E_p = 6$ keV, landing energies of electrons $E_L = 3000$ eV, 1000 eV, 500 eV, working distance WD = 9 mm, primary current $I_p = 150$ pA.

References:

- [1] Müllerová I., Frank L., Advances in imaging and electron physics **128** (2003), p. 309-443.
- [2] Müllerová I., Hovorka M., Hanzlíková R., Frank L., Material Transactions **51** (2010), p. 265-270.
- [3] This work was supported by the GAASCR project no. IAA100650902. The authors would like to thank to Mr. J. Sobota and to Ms. Renáta Hanzlíková for preparation of the sample.

RECENT DEVELOPMENTS AND IMPROVEMENTS OF EOD PROGRAM

B. Lencová

Institute of Scientific Instruments of the AS CR, v.v.i., Královopolská 147, 612 64 Brno,
Czech Republic,
e-mail: bohunka@isibrno.cz

1. Introduction

EOD is used for computations in particle optics that require accurate determination of 2D electrostatic and magnetic focusing, deflection and multipole fields and accurate evaluation of optical properties from aberration theory or from ray tracing. EOD not only allows these types of computations, but it is a complete workplace equipped with a user interface for editing input data for FEM, computation of paraxial trajectories and aberrations and ray-tracing, running the computations, producing graphical outputs and processing them [1]. EOD runs on PCs under Windows XP and newer operating systems or in WINE under Linux. The program has been extended with new plug-ins and continuously improved.

2. First order finite element method

The method we use is the first order finite element method (FEM) with correct computation of the coefficients of the FEM equations for all relevant 2D problems plus error estimations for lenses with rotational symmetry. A more detailed discussion of the accuracy issues is covered in the previous papers from these seminars and at CPO conferences. The many years of use of the EOD and the older FEM software by many users shows that almost all problems with the computation arise simply from an incorrect specification of input data by the user, in particular that of the coarse mesh. The wrong mesh is a typical user problem – in case of coarse mesh they try to use as few mesh lines as possible. But the “recipe” for the coarse mesh is simple: use lines as far as possible parallel with the axis of rotational symmetry. For the fine mesh avoid abrupt changes of mesh density in critical parts of the lens where the field change is large. This is trivial to make and see with a user interface.

For example, in one of the published data [2] we encountered a degenerate quadrilateral, non-physical behavior of magnetic materials plus a mesh with a small number of mesh points in the critical saturated part of the lens; however, back in 1981 5000 mesh points were considered a large number. The next source of problems is the fine mesh, which we solve by the use of a graded mesh step in the fine mesh. The most visible errors in the axial flux density are in the places where the mesh step changes by a factor of 2 or more, and the use of piece-wise constant step used in the original programs increases the required mesh size. Because the PCs are now so fast, there is no need to use obsolete old-type meshes, and the typical mesh sizes can be 80000 points for a magnetic lens and 200000 points for an electrostatic one. Moreover, the computation of “error of potential” gives a clear indication if there is something wrong. This problem will be illustrated on the lens from [2].

The simple topology makes the computation faster and easier and, as a rule, much more accurate than the “standard” FEM with triangular meshes. EOD allows the coarse mesh with practically unlimited number of coarse mesh lines, and this could in principle allow the input of complete microscope geometry into a single computation. The fine mesh with graded mesh step is automatically generated from one or more “gaps” containing user-specified number of fine mesh lines. The number of fine mesh points can be very large. With an ever increasing computation speed of personal computers, a typical field computation is around a minute for $\frac{3}{4}$ million points or for several excitations of a magnetic lens with 80000 mesh points.

3. Optics and ray tracing

Having accurate fields, the attention is naturally shifted from field problems to ray tracing. The paraxial trajectories and the lowest aberration coefficients are computed in a fraction of a second. The next immediate implication of the high accuracy of the available field is in ray tracing, limited before by the inaccuracies of 2D interpolation in meshes with a low number of points. Axial potential or field is interpolated in EOD with cubic or quintic splines, used also in 2D if the mesh is rectangular, or with the well-established ZRP method. Standard 4th-5th order variable-step Runge-Kutta method is applied for paraxial trajectories and aberrations and higher order (7th-8th order Runge-Kutta-Fehlberg) for ray tracing, to name only the most frequently used ones.

In large smooth meshes the accuracy of the ray tracing results can be very high, so that we can easily and correctly derive from the final positions the geometrical aberration coefficients of the 5th order and the chromatic aberrations of the 4th rank, demonstrated in [3], where we have analyzed the aberration coefficients published by Liu [4] and found an order of magnitude discrepancy in only one of the three 5th order field curvature coefficients, in principle an unimportant one. What the author did not find from his coefficients is that the 5th order aberrations demonstrate themselves only if the beam fills a significant part of the lens. Figure 1 shows the geometry of the lens with a unit diameter and ray tracing with the maximum angle of 0.075 rad. Figure 2 shows, in the Gaussian image plane, the comparison of ray tracing with the fit (using up to 7th order terms) and with the geometrical aberrations including only the 5th order terms.

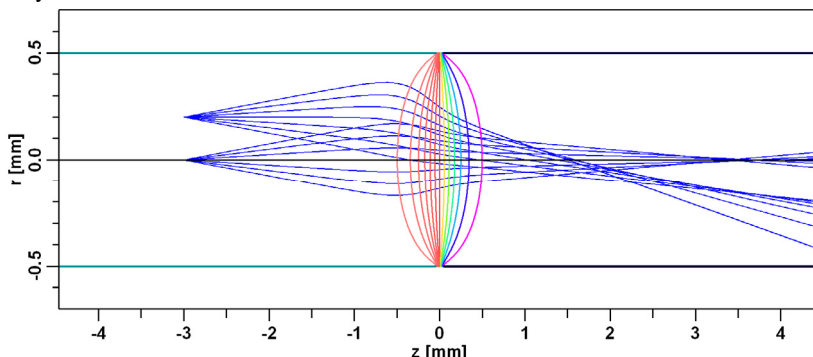


Fig. 1: Lens, equipotentials and rays in the 2-cylinder lens studied by Liu [4].

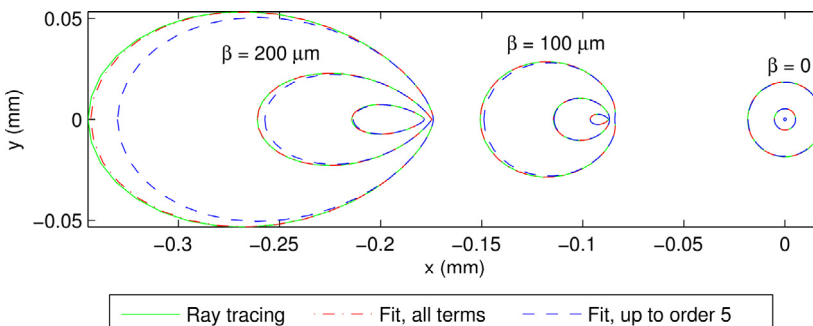


Fig. 2: Gaussian image plane – ray traced results and the effect of aberrations (by M. Oral).

4. EOD accuracy examples

In older papers on electron optics and lens computations suitable data to be used for comparison are often not available; see Hawkes and Kasper for the references before 1986. For example, the low number of mesh lines resulted often, for complicated lens geometry, in a difficult task like a quite complex puzzle to draw a mesh. The “unimportant” parts of the mesh like the coil and the outer magnetic circuit were minimized and the study concentrated on the polepiece region. The next problem, the quality of subdivision into fine mesh with a piecewise constant step, was largely underestimated, because the errors were hardly visible in the result and the trivial check of the validity of the Ampere law was done only in our program LENS thanks to Tom Mulvey. Figure 3 shows the difference in the mesh used by Tsuno and Honda [5] and our mesh. At CPO5 and CPO6 we have shown that the error of the field on axis can be lower than 0.1 % and that the problems reported in [5] are both due to wrong coefficients and fine mesh used for this magnetic lens.

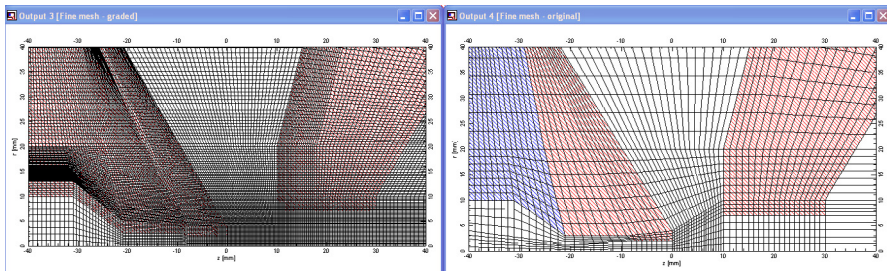


Fig. 3: The difference in the coarse and fine meshes as it is used by us (left) and in [5] (right). The main point in the original paper [2] was the discrepancy in $B(z)$ at -8.5 mm. Already at EUREM in 1996 we (myself, Tom Mulvey and K. Tsuno) have shown that the rearrangement of fine mesh, the increase of the number of mesh points to 14000 points (from original 5500) and the use of our program LENS even in the original mesh provided correct results. However, this fact was omitted in both editions of Jon Orloff's Handbook of Charged Particle Optics, CRC Press 1997 and 2008.

Triple pole-piece lens of Tsuno and Harada

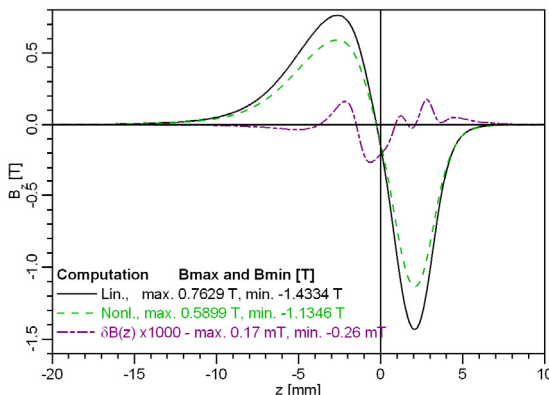


Fig. 4: Flux density on the axis for ± 3500 A-turns excitation if the magnetic materials would not saturate (full line) and for saturated materials (dashed line) computed in EOD for the triple polepiece lens [2]. The shape of both curves is the same and the decrease of the axial field is due to the saturation in the central part of the lens. The dash-dotted curve shows the accuracy of the computation, around 0.02%.

As another example let us take the triple polepiece lens studied by Tsuno and Harada in 1981 [2], which could replace the final projector lens and eliminate the spiral distortion in a TEM. Then the maximum size of the mesh was just 5000 points and the coarse mesh was limited to 15x15 lines. The combination of the low number of mesh lines and points resulted in an inaccuracy of the computed results. We have recalculated the lens in EOD. Figure 4 shows the flux density $B(z)$ on the axis for ± 3500 A-turns: one curve is for hypothetically non-saturating materials, and the other one is for the real saturating materials (soft iron of the yoke and permendur of the pole-pieces). The shape of $B(z)$ almost does not change and its decrease by 20 % is caused by the saturation of the central part of the magnetic yoke (1.8 T) and the central pole-piece (2.35 T). We used over 100000 mesh points (instead of 5000 in [2]) and a much better coarse mesh.

5. Recent improvements

In the ten years of its existence the EOD program has been undergoing a continuous development and improvements of its functionality. For example, DXF files or EODplt files with contours of design can be used as a background to simplify the input of the coarse mesh. Outlines of the elements can be saved as DXF for mechanical engineers. The tracing module of EOD outputs the results also to CSV files of Excel. Ray tracing in computed fields provides graphical outputs of results like trajectories and fields plus intersections with selected planes to EODplt files or graphical windows that can be printed or exported to EMF or BMP files.

Extensive documentation on more than 500 pages gives both the user manual, theory behind FEM, optics and ray tracing and basic description of examples. The easy start in using the program is enabled by a series of PowerPoint presentations and a number of videos, showing the work with EOD on both simple and difficult examples. More than 30 projects with sample data allow the user to understand the work with EOD. Demo version of EOD, allowing the computation with a limited number of mesh points in the FEM mesh, is available on request.

6. Conclusions

The applications of EOD are ranging from detector design via computations of individual lenses to systems and their optimization. In order to facilitate the application range of the program, we have added several plug-ins:

- 1) Computation of space-charge limited high-current electron guns.
- 2) Computation of interactions of electrons with gas in the specimen chamber of the environmental SEM.
- 3) Tolerancing (in development, to be presented at CPO8) [6].

Soon we also plan to switch to a newer Intel compiler to utilize the multi-core architecture of Intel processors and 64-bit operating systems.

References

- [1] Lencová B. and Zlámal J., *Phys. Procedia* **1**(2008), 315-324.
- [2] Tsuno K. and Harada Y., *J. Phys. E: Sci. Instrum.* **14**(1981), 955-960.
- [3] Oral M. and Lencová B., *Ultramicroscopy* **109**(2009), 1365-1373.
- [4] Liu Z. X., *Ultramicroscopy* **106** (2006), 220-232.
- [5] Tsuno K. and Honda T., *Optik* **64** (1983), 367-378.
- [6] Supported by Grant Agency of the AS CR, grant IAA100650805.

COMPARISON OF TECHNIQUES FOR DIFFRACTION GRATING TOPOGRAPHY ANALYSIS

M. Matějka, A. Rek, F. Mika, T. Fořt, J. Matějková

Institute of Scientific Instruments ASCR, Královopolská 147, 612 64 Brno, Czech Republic
e-mail: mmatejka@isibrno.cz

The Diffractive optic elements (DOE) could be composed from periodic gratings for example by the electron beam lithography. When diffraction grating is made there is information about grating topography which is necessary to acquire to control and tune exposition process and development process of exposed resist. The information we are interested for is grating height, crumb and cross section profile. Those data is useful from aspect of the DOE diffractive efficiency determination, when the efficiency is dependent on the grating height, crumb and shape of the grating (sinusoidal, binary, quasibinary, etc.).

There are a wide range of analytical techniques which may be used for surface structure characterization. For high resolution surface investigations, two commonly used techniques are Atomic Force Microscopy (AFM) and Scanning Electron Microscopy (SEM) [1]. Both techniques are capable resolve surface structure down to the nanometer in scale. However the mechanism of topography imaging and type of information acquired is different.

The three-dimensional nature of the AFM can be used to image morphology of samples and enable precise measuring of surface variance in height it also enable to calculate roughness of the surface. Unlike the SEM the AFM operate at air conditions and it doesn't require conductive samples. On the other hand there is some limitation of the AFM compared with the SEM like area of view (typically up to 100 μm x 100 μm) and features height maximum which can be imaged (up to few microns). There is also limitation of the AFM when high aspect ratio structures and structure with high slope is measured. Then on the sharp edges of the relief structure the AFM probe won't be able imaging the real angle of the edge and it would more likely image the probe shape instead. Those known problem of the AFM imaging is called the image artifacts and they are linked at most to the unideal shape and size of the scanning probe.

The SEM imaging allows us identification of changes in slope on the measured structure. In the image they are shown as areas with the higher intensity because the emission of electron from the sample surface on the edges of relief structure is much higher. However, it can be sometime difficult to determine if the imaged future sloping up or down. Another problem is to measure the exact value of variation of the surface in height without tilting of the sample. Sometime there is only option which would be to cleave the sample through the features and look at the sample in cross section, however for cost of the general sample destruction.

Samples for testing of surface imaging by the AFM, SEM and confocal laser scanning microscopy (CLSM) techniques were made. The First sample consist of leaks created in the silicon [111] by anisotropic etching of the silicon in KOH (40%_{wt}) solution through thermal SiO₂ mask. Anisotropic etching was chosen because created structure has given shape, which came from crystallography of the used substrate and different etching rate in different crystallographic direction [2]. This sample was used for SEM JSM-6700F JEOL and AFM Nano-R lateral resolution comparison as well for localization of imaging artifact for the AFM technique. The second sample consist of periodic gratings created in the silicon [100] by the

CF_4 based reactive ion etching (RIE) through negative tone resist (SU-8 2000) mask which has been prepared by the e-beam lithography. Purpose of this sample was to compare imaging of the AFM, the SEM and the CLSM techniques and find method which would be optimal for the diffraction grating profile measurement. For the technique comparison, feature of binary periodic grating ($\Lambda = 4\mu\text{m}$) were chosen.

The Figure 1 shows the SEM and the AFM images of anisotropic etched silicon [111] taken with about the same magnification. Both images show similar surface structure and when we compare size and shape of the etched features in silicon at the images we find out that both is about the same. This confirms the idea of about the same lateral resolution of both techniques, but there is situation when one of the chosen techniques can provide more complex information about the sample surface. For example the SEM image of the first sample (see on Figure 1a)) contains precise information about shape and size, but we can't read information about the height of the features and we can't even decide if the etched features sloping up or down. On the other hand we have measurement from the AFM (see on Figure 1b) and 1c)) which provide us with data about features shape. On the hole bottom we can even see small diversion of [111] crystallographic plane in the $<110>$ direction about the 3° which wasn't evident on the SEM image. However there is image artifact which entering into the overall image. Those image artifacts are noticeable at the edges of the features, where vertical sidewalls of the feature should be imaged there is a sidewall with some high angle imaged instead. This is caused by nonzero shape and apex angle of the scanning probe so when the probe trying to copy the feature profile it doesn't allows copy it properly.

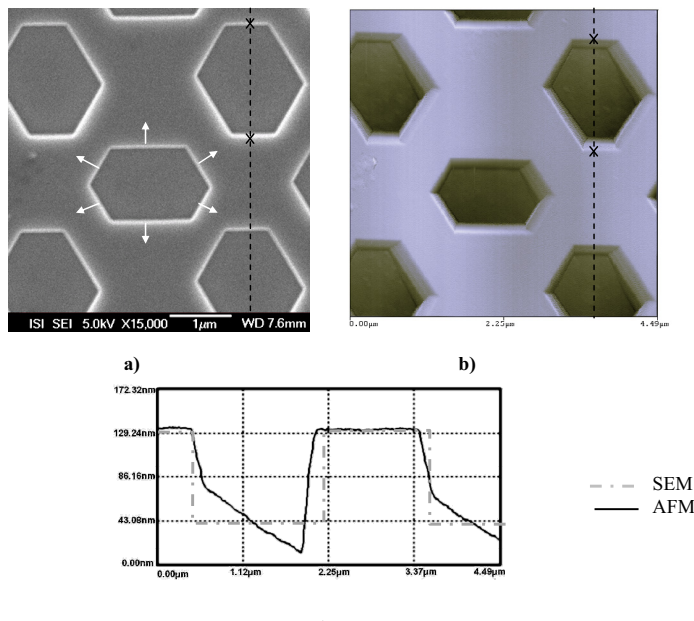


Fig. 1: The sample with the anisotropic etched leaks in silicon [111]: a) SEM image; b) AFM image, c) profile measurement from the AFM with outline of profile from SEM image

On the Figure 2, 3 and 4 we can see AFM, SEM and CLSM image of diffraction grating ($\Lambda = 4\mu\text{m}$) created in silicon by the RIE. From the AFM image (see on Figure 2) or the CLSM image (see on Figure 3) we can get accurate data about the grating height and good conception of its profile and crumb (nondestructive way of observation). From the SEM surface image (see on Figure 4a)) we can retrieve accurate information about the grating crumb and get some conception of its profile (nondestructive way of observation). However from this image we can't obtain any peculiar information about grating height. This shortage could be removed by cleaving of the sample on the feature through and by consequential observation of the arisen cross section (see on Figure 4b)). By this method we could obtain a precise data, about the grating height and profile. However because preparation of the cross section practically means destruction of the general sample, this method isn't applicable in situation when we like keep the sample at full.

To summarize all findings, it looks like the best way to obtain the crucial information, about the diffraction grating profile, height and crumb, after development or etching process, is the combination of the SEM or the CLSM sample surface image and the AFM measurement. From each of those techniques we gather particular information which should match to the real properties of the diffraction grating. By combining of gathered data from SEM and AFM (or CLSM) measurement we can get compact and accurate information about the real diffraction grating topography (see on Figure 5) than if each were the only technique available.

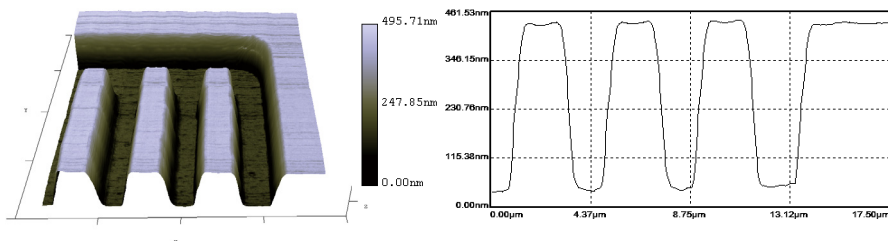


Fig. 2: The AFM image of the sample with periodic grating ($\Lambda = 4\mu\text{m}$) made by CF_4 based RIE in silicon.

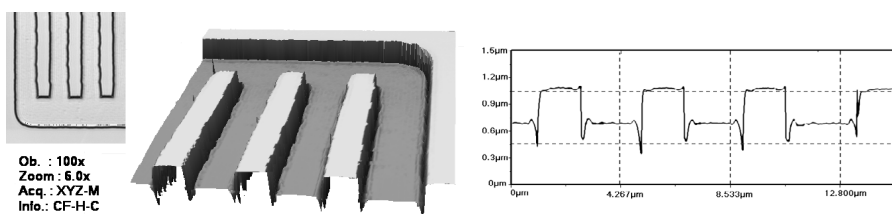


Fig. 3: Image of the sample with periodic grating ($\Lambda = 4\mu\text{m}$) made by CF_4 based RIE in silicon from confocal microscope (CLSM).

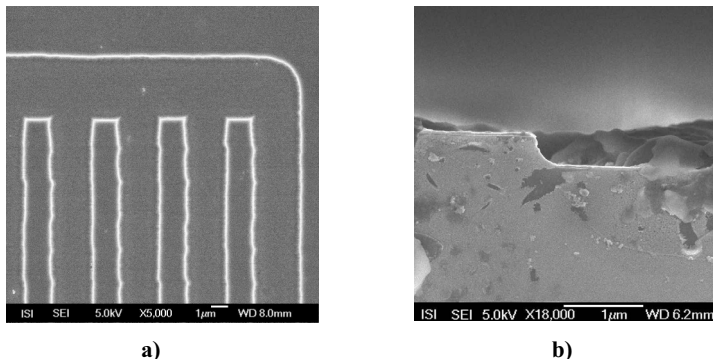


Fig. 4: Image of the sample with periodic grating ($\Lambda = 4\mu\text{m}$) made by CF_4 based RIE in silicon from SEM JSM-6700F JEOL (a) planar image, (b) cross section.

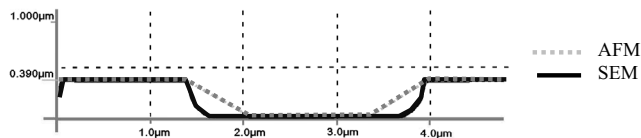


Fig. 5: The profile of the diffraction grating ($\Lambda = 4\mu\text{m}$) from the AFM and the SEM cross-section measurement.

References:

- [1] Russell P., Batchelor D., Thornton J., SEM and AFM: Complementary Techniques for High Resolution Surface Investigations, www.veeco.com.
- [2] Matějka F., The Test specimens for SEM prepared by the electron beam lithography, Bulletin CSEM no. 2 (1993), 20p. 7-12.
- [3] Musil V., Matějka F., Bogr J. Mareček L., Technologické procesy a jejich modelování I (1989), 268p. 248-250.

SUPERCONDUCTIVE PROPERTY AND MICROSTRUCTURE OF MgB₂ / Al COMPOSITE MATERIALS

K. Matsuda^{1*}, M. Mizutani², K. Nishimura¹, T. Kawabata¹, Y. Hishinuma³, S. Aoyama⁴, I. Mullerova⁵, L. Frank⁵ and S. Ikeno¹

¹ Graduate School of Science and Engineering for Research, University of Toyama, 3190, Gofuku, Toyama, 930-8555, Japan

² Graduate School of Science and Engineering for Education, University of Toyama, 3190, Gofuku, Toyama, 930-8555, Japan

³ National Institute for Fusion Science, 322-6, Toki, Gifu, 509-5292, Japan

⁴ Nikkei Niigata, 1572-19, Taroshiro, Kitaku, Niigata, 950-3101, Japan

⁵ ISI Brno, ASCR, Kralovopolska 147, CZ-61264, Brno, Czech Republic

* e-mail: matsuda@eng.u-toyama.ac.jp

Scanning low energy electron microscopy (SLEEM) is a useful tool for observation of insulating samples and determination of microstructure on a specimen surface [1-3]. In our previous studies, metal-matrix composite materials (MMC) have been fabricated on the basis of Al and age-hardenable Al alloys matrices filled with ceramic particles such as Al₂O₃, SiC, and TiC. Their hardening behavior, microstructure, and aging properties have been investigated [4]. Our special technique for fabricating composite materials, 3-dimensional penetration casting (3DPC) method, secures homogeneous dispersion of particles in the matrix without any aggregation and enables one to control the volume fraction of particles within the range of 4 – 50 % even for the particle size below 1μm. So prepared composite materials can be processed by machining, extrusion and rolling. Using the 3DPC method also MgB₂ particles were dispersed in the Al matrix, and the resulting MgB₂/Al composite material was found exhibiting superconductive behavior. We have succeeded in extruding the MgB₂/Al composite billet to a φ 10 mm rod and φ 3 mm wire [5]. In the present work, we have applied the SLEEM to examine the microstructure contrast between boride particles and Al matrix.

MgB₂, AlB₂, TiB₂ and ZrB₂ have all the same crystal structure so MMCs containing equal weights of those particles have been fabricated by the 3DPC method. Also MgB₂/Mg MMC was prepared by a modified 3DPC method. For the SLEEM observation the MMCs were mechanically polished and electro-polished. The basic SEM was the Hitachi S-3500H with a tungsten filament and adaptation to the SLEEM method consisted in introduction of the cathode lens assembly [3].

Figure 1(a) shows demonstration of the SLEEM technique for the MMC containing MgB₂, AlB₂, TiB₂ and ZrB₂ particles. Figures 1(b) to 1(e) correspond to particles labelled (1) to (4) in Fig. 1(a). According to EDS analysis, particles (1) to (4) are particles of MgB₂, AlB₂, TiB₂ and ZrB₂, respectively. Particles of ZrB₂, TiB₂ and AlB₂ are brighter than MgB₂. At majority of the SLEEM conditions the ZrB₂ particles are brightest among all particles. Generally, details of microstructure of particle surfaces were better observable when decreasing the electron energy below 5 keV, however, this trend is not obvious in all cases as shown in Fig. 1(f). For example, certain details were observed on the MgB₂ and ZrB₂ particles at 1 keV.

Also results of the SLEEM examination of MgB₂/Al and MgB₂/Mg MMCs will be included in the presentation and their superconductive properties discussed.

Generally, the SLEEM technique has been confirmed as a useful tool for evaluation of the microstructure of so complicated materials. While the backscattered electron (BSE) signal (see Fig. 1(f)) provides the material contrast enabling one to check the distribution of particles without necessity to perform elemental analysis by X-rays, the SLEEM mode at 1 keV or even below visualizes the microstructure details on individual particles.

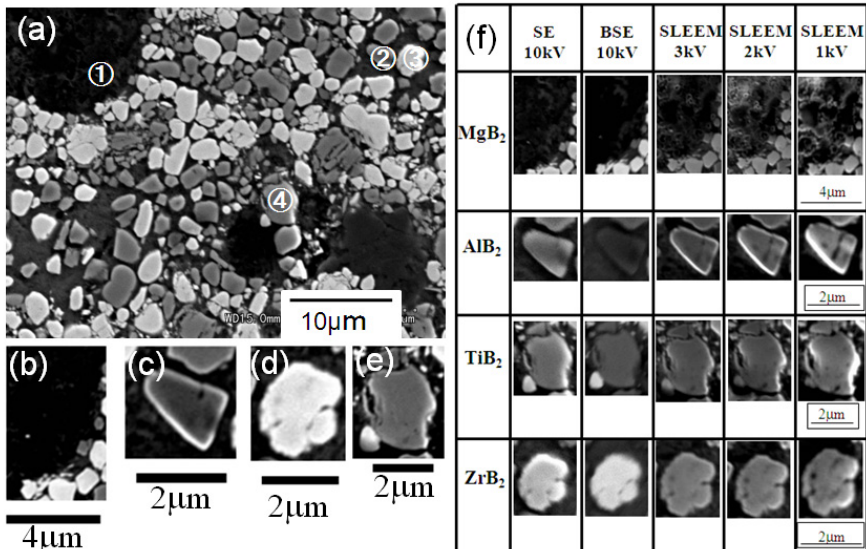


Fig. 1: (a) SLEEM micrograph of a MMC containing simultaneously the MgB₂, AlB₂, TiB₂ and ZrB₂ particles, taken at 5 keV; (b) to (e) are details of particles labelled (1) to (4) in Fig. 1(a); (f) summarizes the SLEEM images of individual particles at various conditions.

Acknowledgement: A part of this work was supported by JSPS-KAKENHI 2008-2010 [Grant-in-Aid for Scientific Research (C) #20560649].

References:

- [1] Frank L. and Mullerova I., J. Electron Microsc. **48** (1999), p. 205-219.
- [2] Mullerova I. and Frank L., Adv. Imaging and Electron Phys. **128** (2003), p. 309-443.
- [3] Matsuda K., Ikeno S., Mullerova I. and Frank L., J. Electron Microsc. **54** (2005), p. 109-117.
- [4] Ikeno S., Matsuda K., Matsuki T., Suzuki T., Endo N., Kawabata T. and Uetani Y., J. Mater. Science **42** (2007), p. 5680-5685.
- [5] Matsuda K., Saeki T., Nishimura K., Ikeno S., Yabumoto Y. and Mori K., Mater. Trans. **47** (2006), p.1-7.

IMAGING OF DOPANTS UNDER PRESENCE OF SURFACE AD-LAYERS

F. Mika^{*}, M. Hovorka and L. Frank

¹ Institute of Scientific Instruments ASCR, Královopolská 147, 612 64 Brno, Czech Republic

*e-mail: mika@isibrno.cz

Scanning electron microscopy is widely used for imaging of semiconductor structures. Image contrast between differently doped areas is observable in the secondary electron emission [1]. Quantitative relation exists between the image contrast and the dopant concentration [2,3,4]. However, further examination has shown the dopant contrast level of low reproducibility and dependent on additional factors like the primary electron dose [5], varying energy and angular distributions of the SE emission [3, 6] and also presence of ad-layers on the semiconductor surface [7].

This paper deals with possible influence of ad-layers on the contrast between p- and n-type doped areas. Under high-vacuum conditions the typical ad-layer consists of the carbonaceous contamination, created owing to decomposition of hydrocarbons under primary beam impact, and of the oxide layer. Experiments have been performed on p-type doped patterns of the dopant concentration varying from $1 \times 10^{16} \text{ cm}^{-3}$ (P16) to $1 \times 10^{19} \text{ cm}^{-3}$ (P19), made on an n-type Si substrate (dopant concentration $1 \times 10^{15} \text{ cm}^{-3}$). The sample was prepared in the clean room laboratory at the Masaryk University, in ON Semiconductor CR factory and at ISI.

The sample was covered with a 20 nm oxide layer. Part of the sample was dipped into the buffered HF and after 45 s slowly moved up. In this way various thicknesses of the oxide layer were formed on the sample surface (see Fig. 1). The sample in its as-inserted status was observed in the Jeol 6700F microscope with a CFE gun and the standard Everhart-Thornley (LEI) detector at the primary energy of 1 keV. The linescan profiles were recorded across the p-type doped stripes in areas with different thickness of the surface oxide layer (Fig. 2).

On the etched sample with the surface covered of only about 1 nm thick oxide layer we can resolve all concentration levels from P16 to P19. At a thicker oxide layer the contrast between the p- and n-type areas has been found reverting for P19 and P18. On the P17 and P16 stripes the signal to noise ratio is too low. On the sample covered with the full 20 nm of oxide we can distinguish the P19, P18 and P17 peaks in the profile. Signal to noise ratio is again too low for the P16 strip. While the P19 and P18 “peaks” are of a similar height, P17 is significantly lower.

Our experiments have confirmed presence of the oxide layer on the doped semiconductor surface significantly influencing magnitude of the secondary electron contrast between the heavily doped p-type areas and the lightly doped n-type substrate. [8]

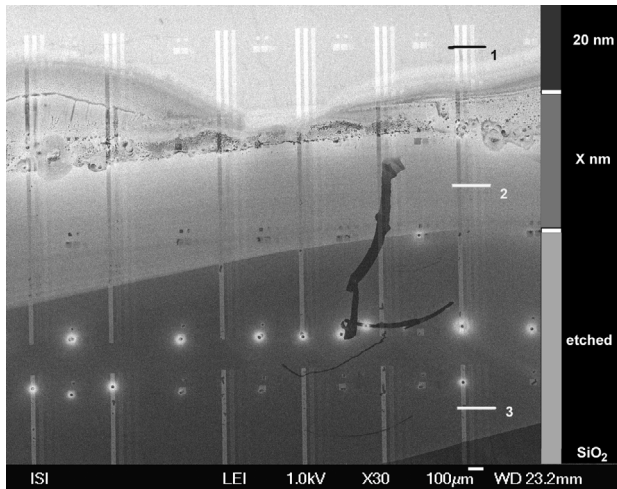


Figure 1: Sample with the p-type doped patterns on an n-type substrate. The sample, covered with an oxide layer (20 nm, X nm, etched) of various thicknesses, is imaged with the LEI detector at 1 keV. Note development in contrast between the p-type doped stripes and the n-type substrate with changes in thickness of the surface ad-layer.

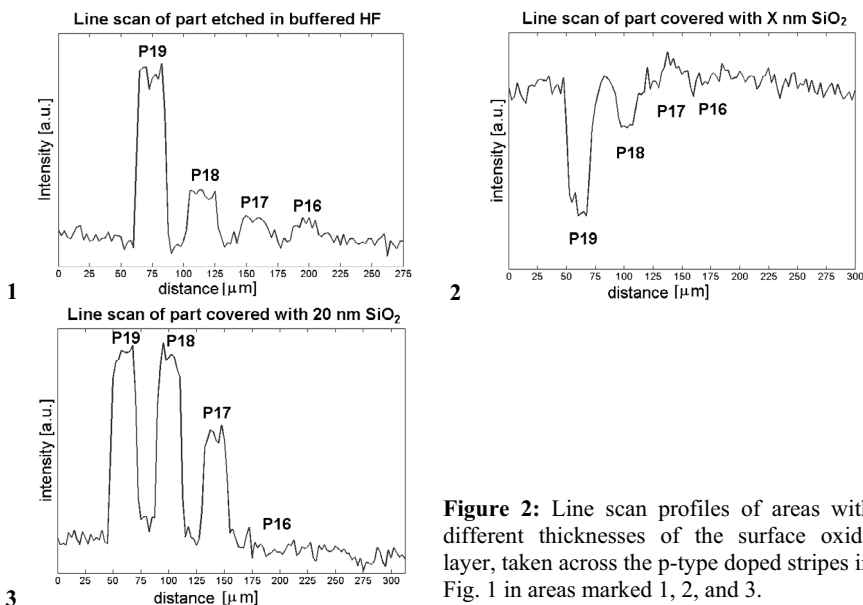


Figure 2: Line scan profiles of areas with different thicknesses of the surface oxide layer, taken across the p-type doped stripes in Fig. 1 in areas marked 1, 2, and 3.

References:

- [1] D. Venables et al., J. Vac. Sci. Technol. **B14** (1996) 421.
- [2] D.D. Perovic et al., Ultramicroscopy **58** (1995) 104.
- [3] I. Müllerová et al., Ultramicroscopy **93** (2002) 223.
- [4] M. M. El-Gomati et al., IEEE Trans. Electron Dev. **51** (2004) 288.
- [5] F. Mika et al., J. Microsc. **230** (2008) 76.
- [6] C. Schönjahn et al., Appl. Phys. Lett. **83** (2003) 293.
- [7] M. M. El-Gomati et al., Surf. Interface Anal. **37** (2005) 901.
- [8] The study was supported by the GACR project no. GP102/09/P543

PROSPECTS OF THE SCANNING LOW ENERGY ELECTRON MICROSCOPY IN MATERIALS SCIENCE

Š. Mikmeková, M. Hovorka, I. Konvalina, I. Müllerová and L. Frank

Institute of Scientific Instruments ASCR, Královopolská 147, 612 64 Brno, Czech Republic

*e-mail: sarka@isibrno.cz

The use of the scanning low energy electron microscopy (SLEEM) has been slowly making its way into the field of materials science, hampered not by limitations in the technique but rather by the relative scarcity of these instruments in research institutes and laboratories. Various techniques exist which are capable of studying the material microstructure, with the scanning electron microscopy (SEM), (scanning) transmission microscopy ((S)TEM) and focused ion beam (FIB) microscopy being perhaps the most known. A specific way to visualizing the microstructure of materials at high spatial resolution, to achieve a high contrast between grains in polycrystals and very fast data acquisition is to use the cathode lens (CL) mode in SEM. The CL mode in the SEM enables us to detect slow but not only slow, high angle scattered electrons that carry mainly crystallographic contrast based on the electron channeling, mostly in the Mott scattering angular range [1].

SLEEM images are very sensitive to crystallographic orientation and perfection of the crystal lattice. The sensitivity to the crystallographic orientation is demonstrated with a series of SLEEM images of the ultra-fine grained (UFG) copper (Fig. 1) taken from the same region with various tilt angles. The benefits of this high sensitivity are clearly demonstrated in Fig. 2 showing the SLEEM images of UFG copper in as-pressed state (Fig. 2a) and after annealing (Fig. 2b). SLEEM provides a tool for determining plastic and elastic strains at the microstructural level with high spatial resolution, and is potentially sensitive enough to strain distribution. Sensitivity assessment is a subject of further research.

The very low energy electron reflectance is promising as an alternative to the electron backscattered diffraction (EBSD) method owing to its high resolution and very fast data acquisition. Fig. 3 shows the reflectance curves acquired by measuring the average image signals over three copper grains with different orientation. Future development of the method should incorporate creation of a database of the reflectance curves to be used as reference “fingerprints” for recognition of grain orientations in the SLEEM micrographs [2].

Good prospects of the SLEEM in materials science follow from many opportunities the method provides not only in fundamental research but also in analytic study of materials.

References:

- [1] I. Müllerová and L. Frank, *Adv. Imaging Electron Phys.* 128 (2003) 309-343.
- [2] Š. Mikmeková et al., *Materials Transactions* 52 (2010) 292-296.
- [3] The project is supported by the EUREKA project no. OE08012.
Mr. Pantlejev and Mr. Man of FME TU Brno kindly provided the specimens of UFG copper.

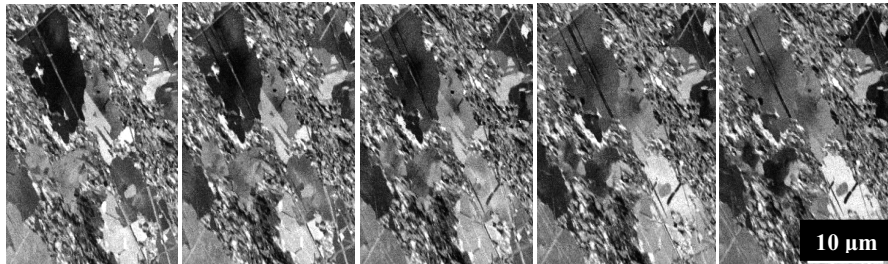


Figure 1: SLEEM images of UFG copper obtained at 2 keV at a specimen tilt 0° , $0^\circ 28'$, $0^\circ 58'$, $1^\circ 24'$, $1^\circ 52'$.

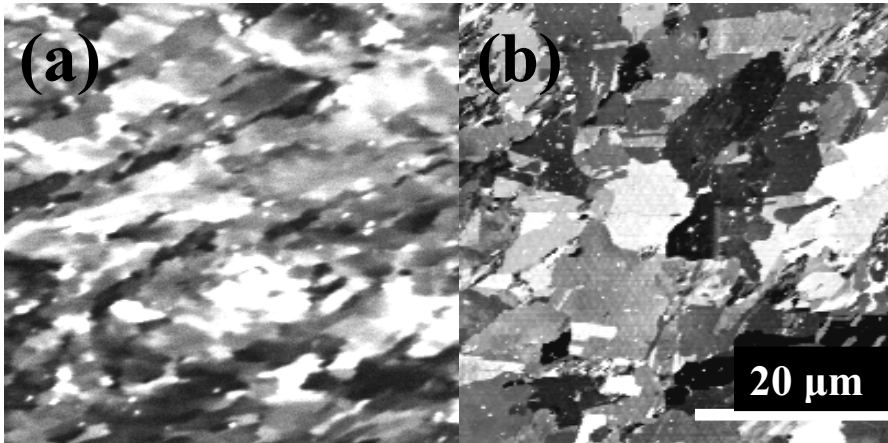


Figure 2: SLEEM images of UFG copper obtained at 10 eV in as-pressed state (a) and after annealing (b).

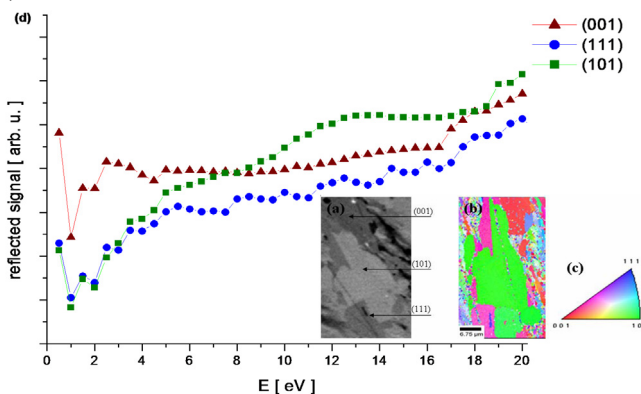


Figure 3: SLEEM image at 11 eV (a), together with EBSD map of the same area (b), the color key for the map (c) and the reflectance curves for three copper grains (d). (Reproduced from [2]).

IMPROVED ABERRATION CORRECTORS FOR THE CONVENTIONAL AND THE SCANNING TRANSMISSION ELECTRON MICROSCOPE

H. Müller, M. Haider, P. Hartel, S. Uhlemann, and J. Zach.

Corrected Electron Optical Systems GmbH, Englerstr. 28, 69126 Heidelberg, Germany
e-mail: mueller@ceos-gmbh.de

During the last decade aberration correctors have become a well-accepted tool in high-resolution electron microscopy. During this time the number of aberration-corrected TEMs installed world-wide has increased from only one to almost 200 systems but also considerable progress in instrumentation and application could be achieved.

The present day commercially available systems are different from the first prototypes in many aspects improving both performance and usability. E.g. a new design for the STEM hexapole corrector with strongly reduced fourth- and fifth-order axial aberrations has been put into practice in 2007 [2,3]. This corrector almost eliminates the intrinsic six-fold astigmatism which was for a long time considered a fundamental limitation of hexapole-type correctors. Within the framework of the TEAM project with this corrector it was possible to demonstrate spatial resolution of better than 50pm at 300kV [4].

The next major step was taken in 2008 with the realization of the first quadrupole-octupole corrector allowing for the simultaneous correction of the spherical aberration Cs and the chromatic aberration Cc for beam energies up to 300kV [5,6]. A considerable improvement of the linear contrast transfer at 80kV from 160pm to 80pm could be demonstrated [7]. This entirely new aberration corrector uses crossed electro-static and magnetic quadrupole fields placed at strongly anamorphic intermediate planes to correct for the axial chromatic aberration. Further magnetic multipole fields are used to compensate for third- and higher-order axial aberrations. An achromatic CTEM equipped with a Cs/Cc-corrector allows for almost aberration-free imaging up to the information limit. The defocus does hardly change for energy offsets of several hundreds of eV, since the system is not just achromatic but also apochromatic. We expect that in addition to the improved information limit for lower acceleration voltages the ability to transfer extended energy windows without loss of resolution will be a strong benefit for electron spectroscopic imaging and biological applications, where rather thick specimens with low-Z material cause strong inelastic scattering.

Recently, new concepts for hexapole-type Cs/B3-correctors have been proposed which compensate for the third-order off-axial coma B3 of the magnetic objective lens including its azimuthal component [8]. This results in an increase of the usable high-resolution field of view by about a factor of five. The novel hexapole Cs/B3-corrector consists of three principal hexapole elements. The correction of the azimuthal off-axial coma is performed by two rather weak pairs of hexapoles situated close to the intermediate image planes of the corrector. These elements are rotated by 30° with respect to the Larmor-transformed principal sections.

An aplanatic CTEM equipped with a Cs/B3-corrector also allows to correct for parasitic off-axial aberrations of second order and is free of limiting fourth- and fifth-order axial aberrations.

References:

- [1] H. Müller, S. Uhlemann, P. Hartel, and M. Haider, Aberration-corrected optics: From an idea to a device. Proceeding of CPO-7 (Eds. E. Munro and J. Rouse), Physics Procedia **1** (1), 167-178 (2008).
- [2] H. Müller, S. Uhlemann, P. Hartel, and M. Haider, Advancing the hexapole Cs-corrector for the scanning transmission electron microscope. Microscopy and Microanalysis **12** (6), 442-455 (2006).
- [3] P. Hartel, H. Müller, S. Uhlemann, and M. Haider, Experimental set-up of an advanced hexapole Cs-corrector. Microscopy and Microanalysis **13** (suppl. 2), 1148-1149 (2007).
- [4] R. Erni, M. D. Rossell, C. Kisielowski, and U. Dahmen Atomic-resolution imaging with a sub-50-pm electron probe. Phys. Rev. Letters **102**, 096101 1-4 (2009).
- [5] M. Haider, H. Müller, S. Uhlemann, U. Löbau, and R. Höschen Prerequisites for a Cc/Cs-corrected ultrahigh-resolution TEM. Ultramicroscopy **108** (3), 167-178. (2007).
- [6] P. Hartel , H. Müller , S. Uhlemann , J. Zach , U. Löbau , R. Höschen and M. Haider, Demonstration of CC/CS-correction in HRTEM in: Proceedings of EMC 2008 (1) (Eds. Luysberg, K. Tillmann, T. Weirich), 27-28 (2008).
- [7] M. Haider, P. Hartel, H. Müller, S. Uhlemann, and J. Zach Information transfer in a Cc/Cs-corrected Transmission Electron Microscope. Microscopy and Microanalysis, *accepted for publication* (2010).
- [8] M. Haider, H. Müller, and S. Uhlemann, Present and future hexapole aberration correctors for high-resolution electron microscopy. in: Advances in Imaging and Electron Physics (Ed. P.W. Hawkes) 153, 43-119 (2008).

TRANSMISSION MODE IN SCANNING LOW ENERGY ELECTRON MICROSCOPE

I. Müllerová*, M. Hovorka and L. Frank

Institute of Scientific Instruments of the ASCR, v.v.i., Královopolská 147, 612 64, Brno,
Czech Republic

*e-mail: ilona@isibrno.cz

High resolution imaging of thin foils with a signal transmitting the sample irradiated by high energy electrons up to hundreds of keV in the transmission electron microscope routinely shows individual atomic columns or even single atoms. The scanning electron microscope (SEM) operates at units or tens of keV, imaging the sample in the reflected signal. High resolution SEM, utilizing the “in-lens” system and a corrector of aberrations, has recently also achieved imaging of single atoms [1] and the transmitted mode at tens of keV appears more and more frequently [2].

We incorporated the cathode lens (CL) principle, well known from the emission microscope, to the SEM [3] in order to operate at very low landing energies. The primary beam electrons of several keV are decelerated to nearly zero energy of landing on the specimen negatively biased to high potential. Reflected electrons are collected on a grounded detector situated above the sample but the same can be done below the sample of a fair transparency for electrons [4]. High collection efficiency and high amplification of both detectors is secured thanks to the cathode lens field. We use a scintillation detector for the reflected mode and a semiconductor structure for the transmitted electron (TE) mode. In this arrangement resolution of few nm is obtainable across the full energy range [5].

In Fig. 1 the TE mode is demonstrated on a 3 nm carbon film deposited on the holey carbon substrate supported by a standard copper grid at various landing energies. Near 350 eV the carbon film transmitted signal exhibits an increase over the full primary flux passing holes in the carbon substrate due to contribution of secondary electrons released near the bottom surface of the sample. A detector version capable of suppressing this “incoherent” component has been designed and tested.

In the very low energy range we rely on the inelastic mean free path of electrons steeply extending below about 50 eV and hence on the increased penetrability of electrons, at last through crystalline layers. While at tens of keV the standard thickness and material contrasts are available, the image contrast at units of eV is influenced by electronic structure of the sample. One of the demonstration experiments were done on a sample of mutually overlapped graphene layers with some single layer islands, deposited on a supporting grid. The micrograph in the total transmitted signal at very low energy, shown in Fig. 2, exhibits a very high thickness contrast, obviously sensitive to individual atomic layers. When measuring the energy dependence of the transmitted signal we found the maximum transmissivity at 5 eV. The same field of view in the reflected mode is shown for comparison. Similar results have been obtained with a 3 nm foil of gold [4].

Let us mention that no problems were faced as regards conductivity and stability of the small pieces of foils when irradiated and transmitted by the focused electron beam. Also the initial

fear of formation of “microlenses” owing to penetration of the strong electrostatic field into holey foil eyes and of their undesirable affecting the primary beam properties has not confirmed.

The method looks promising for electron spectromicroscopy in the transmitted mode at very low energies especially when a multichannel detector is used. [6]

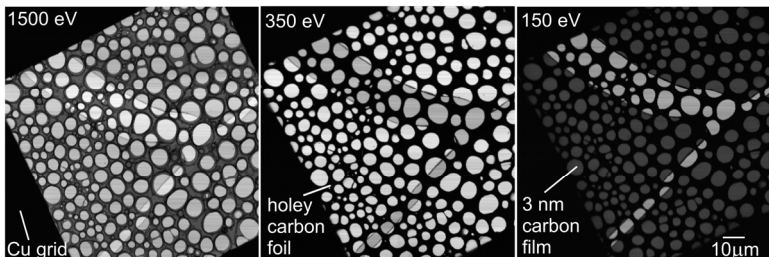


Fig. 1: The TE mode micrographs of a 3 nm carbon film on a copper grid covered by a holey carbon foil; landing energies of electrons as indicated. (Sample provided by H.-W. Fink, University of Zürich, leader of the SIBMAR project.)

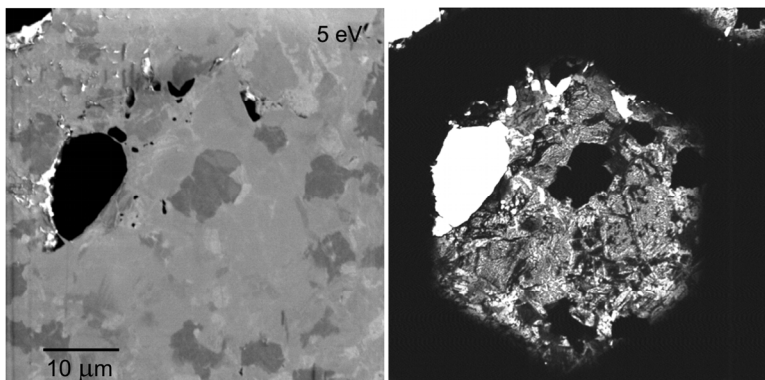


Fig. 2: Graphene deposited on a supporting grid shown in the BSE mode (left) and in the total TE signal (right); primary beam energy 6 keV retarded to the landing energy of 5 eV. (Sample provided by Andre Geim, University of Manchester).

References:

- [1] Zhu Y., et al, *Nature materials* **8** (2009), p. 808-812.
- [2] Merli P.G., et al., *Ultramicroscopy* **94** (2003), p. 89-98.
- [3] Müllerová I. and Frank L., *Adv. Imaging & Electron Phys.* **128** (2003), p. 309-443.
- [4] Müllerová I., et al., *Materials Trans.* **51** (2010), p. 265-270.
- [5] Konvalina I. and Müllerová I., *this Proc.*
- [6] The work is supported by the GAASCR project no: IAA100650902 and the EU STREP project no. 028326 (SIBMAR, <http://sibmar.org/index.html>).

SIMULATION OF CURVED AXIS SYSTEMS, IMAGING ENERGY FILTERS, BEAM SEPARATORS AND ELECTRON MIRRORS

E. Munro*, J. Rouse, H. Liu and L. Wang

Munro's Electron Beam Software Ltd, 14 Cornwall Gardens, London SW7 4AN, England
 *e-mail: eric@mebs.co.uk

Introduction. Curved axis systems are used in many applications in electron and ion optics, including imaging energy filters [1], monochromators [2], beam separators for LEEM [3], etc. Beam separators are also combined with electron mirrors for aberration correction in LEEM or PEEM [4]. Curved axis systems are more complicated to simulate than straight axis ones, because: (1) The axis path itself must be computed; (2) 3D field computation is often required in bending elements; (3) Iterative adjustment of bending element geometries and fields is often required to obtain the required axis path with stigmatic focusing of paraxial rays; and (4) Aberration formulae are more complicated and higher order aberrations are often required. Electron mirrors, used in combination with beam separators, are also harder to simulate than electron lenses, because traditional paraxial ray and aberration theories break down at the reflection point. Over the last ten years or so, we have been developing several software packages for the simulation of such systems, including FILTER, PRISM, CURVED_IMAGE, MIRROR_DA and SECTION_DA [5]. In this presentation we summarize the status of these simulation packages and suggest some future trends for their further development.

FILTER. This software was developed for simulating imaging energy filters [1]. These contain bending magnets which refract the beam in a curved path, as shown in Fig. 1a.

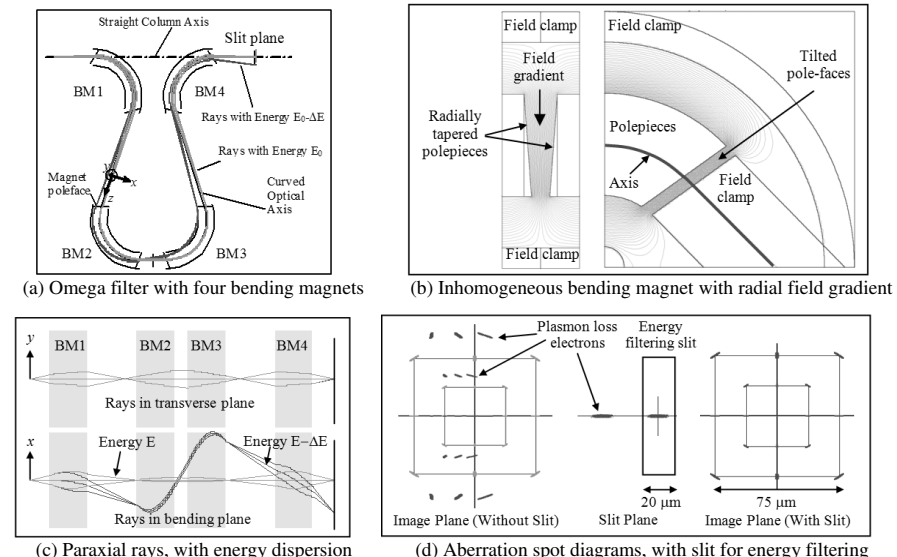


Fig. 1. Simulation of an imaging energy filter with the FILTER software.

The FILTER software handles homogeneous bending magnets, and also inhomogeneous magnets (with radial field gradient in bending plane) such as are used in Mandoline filters [6]. The software first computes an approximate design, based on ideal fringe fields (SCOFF approximation), and then computes real fringe fields by 2D or 3D finite difference method. Axis path and paraxial rays are traced numerically by Runge-Kutta method. Pole-face tilt angles, magnet strengths and separations, etc., are iteratively adjusted to achieve stigmatic focusing along the required axis path. This iterative adjustment is done using damped least squares (“DLS”) optimization [7]. For inhomogeneous magnets, fully 3D fields are computed in the fringe regions (Fig. 1b) for a range of pole-face tilt angles, and this data is supplied to the iterative autofocus algorithm. After autofocus, the paraxial rays can be plotted (Fig. 1c) and the dispersion computed. The second rank aberrations are then computed with the aberration formulae of Rose [8]. Aberration spot diagrams can then be plotted in the image and slit planes (Fig. 1d). This aberration plot shows how the energy filtering slit improves the image quality by removing plasmon loss electrons. The software can simulate a wide range of imaging energy filter designs, including S-filters and W-filters [9].

PRISM. This software was originally developed for designing a beam separator for LEEM [10]. A modified version has also been developed for simulating certain omega filters. The type of magnetic prism considered is shown in Fig. 2a. The prism refracts the beam through 90° , and focusing is achieved using gap fields which are perpendicular to the entrance and exit axes. The focusing effects arise because once the beam starts bending it passes obliquely through the gap fields, which creates quadrupole focusing components. The prism has a very simple geometry, with mid-plane symmetry about the bending plane, distance D between the planar polepieces, and planar gaps of widths S_1, S_2, S_3 , etc. Ideally there should be three such gaps, with independent excitations, to provide the three desired focusing conditions: (1) 90° total bending, (2) stigmatic focus between object and image planes, and (3) stigmatic focus between “diffraction” and “slit” planes. Each gap region has a simple geometry, defined by the polepiece spacing D and its gap width S (Fig. 2a). Assuming the polepiece surfaces are magnetic equipotentials, the field distribution in each gap region can be computed analytically by a Schwarz transformation (conformal mapping) [11]. The axis path (Fig. 2a) and multipole fields (Fig. 2b) are computed, and paraxial rays (Fig. 2c) are traced by Runge-Kutta method, with auto-focusing by DLS [8]. The primary (second rank) aberrations are computed with Rose’s formulae [9]. Higher order aberrations are computed by direct ray tracing through the analytic fields, and can be plotted as aberration spot diagrams (Fig. 2d). Since direct ray tracing is used, discrete Coulomb interactions can also be computed by N-body Monte Carlo simulation [12].

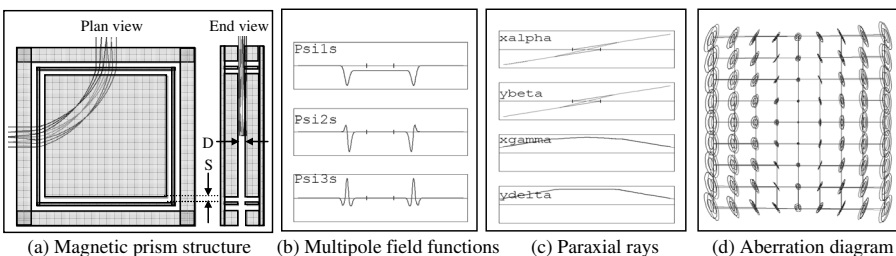
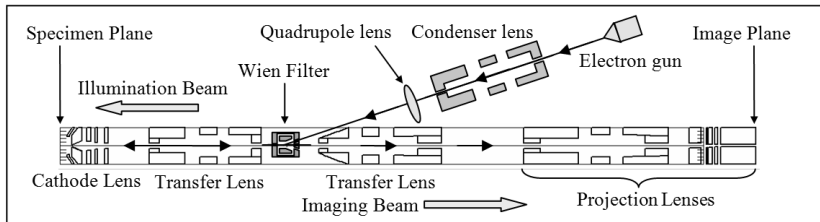


Fig. 2. Simulation of a 90° magnetic prism beam separator with the PRISM software.

CURVED_IMAGE. This software simulates systems with general curved axis elements, with essentially 3D electrostatic and magnetic fields. The curved axis is assumed to lie in a plane. A typical system that can be simulated is shown in Fig. 3a. This is a LEEM system with a Wien filter for separating the illuminating and imaging beams. The dipole fields in the Wien filter are adjusted to give 20° bending of the illumination beam (Fig. 3b), and a straight through condition for the 5 kV imaging beam (Fig. 3c). The quadrupole fields in the Wien filter are adjusted to correct astigmatism in the imaging beam, and an external quadrupole lens corrects astigmatism in the illumination beam. The \mathbf{E} and \mathbf{B} fields in the Wien filter are computed by 3D finite difference method [13] with our CO-3D software [14], and the electric potential $\Phi(x,y)$ and transverse flux density $B(x,y)$ are obtained at the grid points (x_i,y_j) in the bending plane. Values of $\Phi(x,y)$ and $B(x,y)$ throughout the (x,y) plane are fitted by bi-quintic spline interpolation between the grid-point values. The curved axis is computed by a Runge-Kutta ray trace. The axis curvature, $\kappa(z)$, and electric and magnetic multipole field functions, $\phi_{0c}(z) \rightarrow \phi_{4c}(z)$ and $\psi_{1s}(z) \rightarrow \psi_{1s}(z)$, are extracted along the curved axis and fitted with Hermite function series [15]. Paraxial rays are computed in the curved axis coordinate system, and the system is auto-focused by adjusting the field strengths with DLS [8]. The aberrations are then computed by the Differential Algebra (DA) method [16], which can compute the primary (second order) and secondary (third and higher order) aberrations (Fig. 3d). Discrete Coulomb interactions can also be computed by N -body Monte Carlo simulation (Fig. 3e).



(a) A LEEM system with a Wien filter beam separator, with curved axis for the illumination beam and straight axis for the imaging beam. The illumination and imaging optics are simulated with CURVED_IMAGE software.

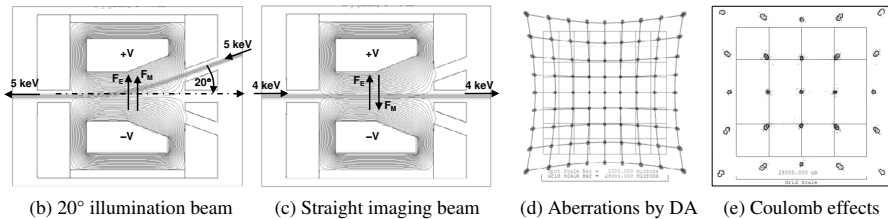


Fig. 3. Simulation of a Wien filter beam separator with the CURVED_IMAGE software.

MIRROR_DA. This software is for simulating electron mirrors. The traditional difficulty of computing paraxial rays and aberrations near the reflection point is eliminated using the formulation of Rose and Preikszas [17], with time t as independent variable, and dependent variables $x(t)$, $y(t)$, $h(t) = z(t) - \xi(t)$, where $\xi(t)$ = reference electron along the axis. The DA method is used to compute the aberrations, using DA quantities $X(t)$, $Y(t)$, $H(t)$ [18]. The accuracy has been checked by comparison with direct ray tracing through fields defined with Fourier-Bessel series. Mirrors have been designed with negative spherical and chromatic aberration and field curvature ($C_s < 0$, $C_c < 0$, $C_{fc} < 0$). An example is shown in Fig. 4.

Initially, we assumed Hermite functions which are anti-symmetric about the reflection plane. However, this condition does not hold rigorously for curved reflection electrodes (Fig.4). This problem was solved by adding symmetric Hermite functions for curved reflection electrodes.

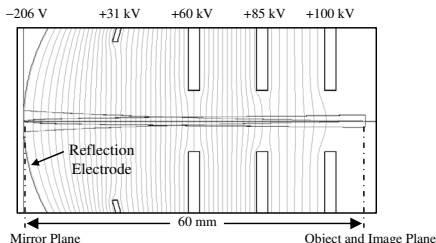


Fig. 4. Simulation of an electron mirror.

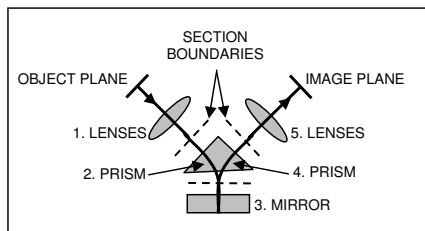


Fig. 5. Concept of SECTION_DA software.

SECTION_DA. This software allows systems with several sections of different types, such as a combination of electron lenses, mirrors and beam separators (Fig. 5), to be analysed as a complete system. The only restriction is that the interfaces between each section must be in field-free regions. Paraxial rays in each section are computed to provide a 2×2 transfer matrix for the paraxial rays, and the system elements are adjust by DLS [8] to achieve autofocus. The aberrations through the entire system are then computed by DA method. This is feasible because the DA method automatically computes all possible aberrations, so it does not matter, for example, that curved axis elements have different aberration symmetries than mirrors.

Future Trends. Proposed software improvements include: (1) Incorporating DA method into the FILTER software, for computing higher-order aberrations; (2) Extending FILTER to handle electric fields, for simulating Ω -filter monochromators [2]; (3) Modifying PRISM to handle more general bending angles than 90° ; (4) Using more general fitting functions than Hermite functions for CURVED_IMAGE; (5) Improving user interactivity and graphical interfaces for the curved axis software; and (6) Using heuristic optimization methods, such as genetic algorithms [19], for improving the design of curved axis systems and electron mirrors.

References:

- [1] H. Rose and D. Krahl, in *Energy-Filtering Transmission Electron Microscopy*, edited by L. Reimer (Springer, Berlin, 1995), pp. 43-149.
- [2] H. Rose, *Geometrical Charged-Particle Optics* (Springer, Berlin, 2009), pp. 360-362.
- [3] H. Rose, see ref. [2], pp. 292-297.
- [4] W. Wan, J. Feng, H.A. Padmore et al., Nucl. Instrum. Meth. Phys. Res. A **519** (2004) 222-229.
- [5] FILTER, PRISM, CURVED_IMAGE, MIRROR_DA, SECTION_DA User Manuals (MEBS, London).
- [6] S. Uhlemann and D. Krahl, Optik **96** (1994) 163-178.
- [7] K. Levenberg, Quarterly of Appl. Math. **2** (1944) 164-168.
- [8] H. Rose, Optik **51** (1978) 15-38.
- [9] H. Rose, see Ref. [2], pp. 369-372.
- [10] M. Mankos, D. Adler, L. Veneklasen and E. Munro, Physics Procedia **1** (2008) 485-504.
- [11] W.R. Smythe, *Static and Dynamic Electricity*, 3rd Edition, (McGraw-Hill, New York, 1968), pp. 73-120.
- [12] T. Groves, D.L. Hammond and H. Kuo, J. Vac. Sci. Technol. **16** (1977) 1680-1684.
- [13] J.A. Rouse, in *Advances in Optical and Electron Microscopy*, edited by T. Mulvey, Vol. **13** (1994) 1-121.
- [14] CO-3D Software User Manual (MEBS, London, 2008).
- [15] M.L. Boas, *Mathematical Methods in the Physical Sciences*, 2nd Ed.(Wiley, New York, 1983), pp. 530-540.
- [16] M. Berz, Particle Accelerators **24** (1989) 109-124.
- [17] H. Rose and D. Preikszas, Nucl. Instrum. Meth. Phys. Res. A **363** (1995) 301-315.
- [18] L. Wang, J. Rouse, E. Munro, H. Liu and X. Zhu, Optik **119** (2008) 90-96.
- [19] R.L. Haupt and S.E. Haupt, *Practical Genetic Algorithms*, (Wiley, New York, 1998).

IMPACT OF A BEAM LIMITING APERTURE ON COULOMB INTERACTION IN A LOW-VOLTAGE FOCUSED ION BEAM SYSTEM

K. Marianowski, T. Ohnweiler^{*}, and E. Plies

Institute of Applied Physics, University of Tübingen,
Auf der Morgenstelle 10, D-72076 Tübingen, Germany

* e-mail: timm.ohnweiler@uni-tuebingen.de

As focused ion beam (FIB) systems are now well established in both semiconductor industry and academic research, the impact of Coulomb interaction (CI) on the resolution of such a system has been studied intensely by many groups. On the one hand there are groups such as [1] which investigate CI in the whole column making some assumptions about the characteristic parameters of the Gallium liquid metal ion source (LMIS), the most commonly used emitter in FIB systems. On the other hand there are people such as [2] who simulate CI in the LMIS (tip to extractor). However, since almost all investigations are limited to systems consisting of two einzel lenses with high landing energies of about 30 keV, it is necessary to also investigate the influence of CI in a dedicated low-voltage FIB system based on immersion optics [3] to be able to further improve this system.

The sample system examined consists of two immersion lenses: A condenser lens, which resembles the optimised lens according to Swanson and Orloff [4], and an objective lens, which has been somewhat modified to meet experimental requirements. The distance between the emitter tip and the first electrode of the condenser lens is 11 mm, the total length of the column is 570 mm and the working distance is 15 mm. Both electrostatic lenses are operated in the internal acceleration mode, i.e. their focus electrodes are set on a potential higher than the potential of the drift space between the two lenses. The final landing energy is 3 keV. In the first step, the system is characterised and optimised in the absence of CI using the commercial software package OPTICS by Mebs Ltd. [5] and the formula for the total geometrical aberration disc presented in [1]. To minimise CI effects beforehand the drift space potential is chosen as high as possible resulting in a kinetic energy of the ions between the lenses of 10.55 keV. Afterwards, the optimised system is analysed and further optimised in the presence of CI using the commercial software package IMAGE by Mebs Ltd. [5]. According to Hagen et al. [6] and Mair et al. [7] an angular current density of 15 μ A/sr, a virtual source size of 50 nm and an energy spread of 5 eV (FWHM) are used to describe the Gallium LMIS. In this step, the beam current is assumed to be 125 pA and kept constant throughout the entire column. As CI in charged particle beams causes a space charge effect, the perturbed final positions of the particles are evaluated in the plane of best focus. The probe size is defined as the disc containing 50% of the total beam current. In the next step, a beam limiting aperture with a diameter of 50 μ m is placed in the drift space 146.2 mm below the emitter tip and the beam current before the aperture is gradually increased. Due to the extremely long calculation time the maximum beam current investigated is 18 nA, although the emission current in the system introduced in [3] is about 2 μ A. Finally, the system is optimised by readjusting the magnification again. As the diameter of the aperture is kept constant, the remaining probe current consequently changes. Results are given in figure 1a).

To confirm the results obtained with IMAGE, Monte Carlo simulations have also been done with MONTEC, a program developed by Jansen [8]. To estimate the impact of CI using MONTEC, the sample system has to be modeled as a succession of drift spaces and uniform acceleration and deceleration zones separated by thin lenses. The latter are positioned using the results calculated with OPTICS. Using MONTEC it is possible to set an aperture, but it stops all particles and the simulation especially for high emission angles because the maximum number of particles is limited to 1500. Therefore our simulations have been done in two steps: Firstly the impact of CI is only calculated up to the aperture. Secondly the CI is only calculated in the region behind the aperture, using the probe current from IMAGE. This verifies that the dominating effect stems from the region up to the aperture, as expected from the high potential of the drift space, the low probe current and the landing energy of 3 keV. The impact of CI from this first region is shown in figure 1b). The combined FW 50 size is defined according to [1]. The required aberration discs are resumed from OPTICS. Figure 1b) shows the same functional dependency with entirely smaller values compared to IMAGE. For examination of the whole column MONTEC has to be recompiled implementing more particles.

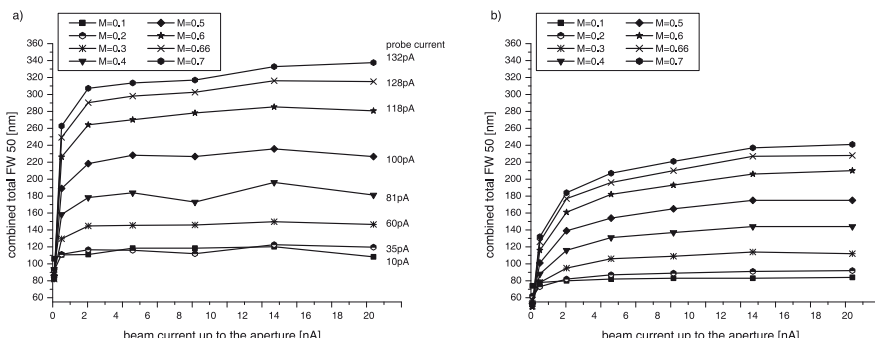


Fig. 1: Combined FW 50 size over the beam current in the region up to the aperture for a landing energy of 3 keV and a kinetic energy between the lenses of 10.55 keV for different magnifications (M) calculated with a) IMAGE and b) MONTEC. Using IMAGE the ions can be traced through the whole column. In this case the aperture limits the beam current to the final probe current. Using MONTEC only the impact of the first region can be calculated.

References:

- [1] Kruit P., Jiang X. R., J. Vac. Sci. Technol. B **14** (1996) 1635-1641.
- [2] Radlčík T., Lencová B., Ultramicroscopy **108** (2008) 445-454.
- [3] Rauscher M., Development of an advanced low energy focussed ion beam system based on immersion optics, Dissertation, 2006.
- [4] Orloff J., Swanson L. W., J. Appl. Phys. **50** (1979) 2494-2501.
- [5] Software by Munro's Electron Beam Software Limited, London, www.meps.co.uk.
- [6] Hagen C. W., Fokkema E., Kruit P., J. Vac. Sci. Technol. B **26** (2008) 2091-2096.
- [7] Mair G. L. R., Forbes R. G., Latham R.V., Mulvey T., Microcircuit Eng. **83** (1983) 171-178.
- [8] Jansen G. H., MONTEC program, Information obtainable from: Particle Optics Foundation Lorentzweg 1, 2628 CJ Delft. The Netherlands. See also Jansen G. H., Coulomb Interactions in Particle Beams, Adv. Electron. Electron Phys., Suppl. **21** (1990).

RAY TRACING, ABERRATION COEFFICIENTS AND INTENSITY DISTRIBUTION

M. Oral^{1*}

¹ Institute of Scientific Instruments, ASCR, v.v.i, Královopolská 147, 612 64 Brno, Czech Republic

* e-mail: oral@isibrno.cz

In particle optics paraxial ray tracing (solution of the paraxial trajectory equation) provides the basic imaging properties of an optical system and real ray tracing (solution of the equation of motion with time as the parameter) gives the complete particle paths including all aberrations. While there are methods of computing the aberration coefficients directly, for example by evaluating the aberration integrals, ray tracing can also be used for this purpose. The calculation is based on linear regression of the aberration polynomials on data of ray tracing [1]. This method can be applied to any optical system using a general multivariate aberration polynomial fulfilling conditions required by the symmetry of the particular optical system (chapter 23 in [2]). Furthermore, the statistical significance of the individual aberration coefficients can help to identify the aberration terms that are the most important in the particular case. The aberration polynomial with known aberration coefficients can be used for fast evaluation of particle positions in a given reference plane. The high calculation speed (about 10^7 particles per second per one CPU core) makes it feasible to simulate the current density (intensity) distribution in a reference plane (about 10^9 particles are needed to construct a 2-D current density profile). This is a useful tool for optimization of the probe size and shape in focused-ion instruments. We present an example of an optimization of liquid gallium-ion system with a tilted sample and an extraction field of a secondary ion analyzer. The basic imaging conditions in the tilted sample plane are set using a paraxial optimization. Ray tracing, regression analysis and the calculation of the intensity distribution are used to tune the system for the required (circular) spot shape.

Ion-optical columns are mostly constructed to produce a circular spot on a sample which is perpendicular to the axis of the optical system. If the plane of the sample is tilted, the rotationally symmetrical beam creates an elliptical spot, which can be further elongated by an electrostatic field of a secondary ion detector, spectrometer or an analyzer. As a result, the spot becomes astigmatic to a level which cannot be corrected using the common stigmator. A suitable correction method was developed, which allows to compensate for both the ellipticity due to the tilt and the extracting field and to achieve a circular spot on the titled sample. The compensation is provided by a suitable setting of two correcting quadruples and by refocusing the objective lens. The required settings of the quadrupole excitations and objective lens are obtained by a paraxial optimization.

Initially, the optical system contains only the fields of the lenses, the deflectors and the fields near the sample. Selected trajectories in such a system, computed in EOD [4], are shown in Fig. 1. The optimization procedure is based on the assumption that the correcting fields cause certain perturbation to the optical system and its purpose is to fulfill necessary conditions (stigmatic imaging, position of the Gaussian image plane, shape of the image).

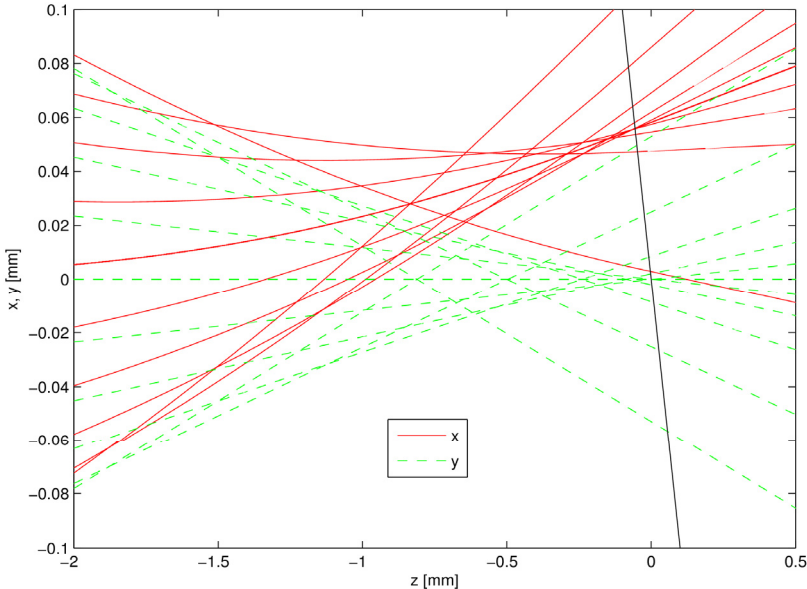


Fig. 1: Uncorrected trajectories in the vicinity of the titled sample. The particles were started on axis in the plane of the virtual source. The inclined straight line shows the intersection of the planar sample surface with the x-z plane. The trajectories are deflected in the x-direction by the extracting field of the detector of secondary ions.

The electrostatic potential in the vicinity of the optical axis can be expressed as a series expansion in the transversal coordinates x and y (chapter 7 in [2]). The series expansion contains axial field functions of the rotationally symmetric, dipole and quadrupole potential (the higher multipole components do not influence the paraxial trajectories). According to Rose [3], to obtain a stigmatic and uniformly magnified image in the presence of a quadrupole field, two other separate independent quadrupoles are needed. The ability to change the focusing of the objective lens adds another free parameter and provides the necessary flexibility. Often the optical column contains a two-stage deflection system. The deflection dipole field of each of the deflection stages is generated by an eight-pole electrode system, which can be used to create the correcting quadrupole field.

The optimization computation starts with solving the paraxial trajectory equation with the initial fields. The optimization is then run iteratively. The correcting fields are assumed to create a small perturbation represented by a set of perturbation parameters. In each iteration better estimates of the perturbation parameters are calculated, which leads to a more accurate solution of the perturbed paraxial equations. The procedure is terminated after the optimization conditions are met with sufficient accuracy. The shape of the spot is controlled by the ratio of the magnifications in the two perpendicular principal sections (defined for systems with quadrupoles, [3]). The spot shape is verified by ray tracing and by calculating the intensity distribution in the beam, which also includes the effect of geometric and chromatic aberrations.

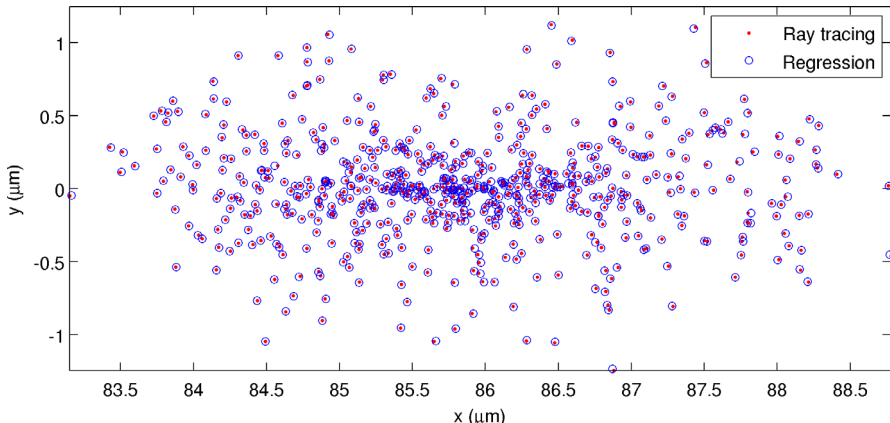


Fig. 2: Positions of particles on the tilted target computed by ray tracing in EOD and by the aberration polynomials with coefficients determined by regression analysis. The initial conditions of the particles were generated so that positions on the virtual source and in the aperture were random with a uniform distribution within circles and the energy values were uniformly random.

Ray tracing, performed in EOD, is used to determine the coefficients of the paraxial imaging and of the aberrations using the technique described in [1]. Since the system has one plane of symmetry, the aberration polynomial consisting of various mixed terms in initial slope, position and relative energy deviation, has 70 terms: one constant (zeroth-order) term (paraxial deflection), 4 paraxial first-order terms and one first-rank term (energy dispersion), 34 geometric terms of orders two and three and 34 terms of rank 4 (linear in the relative energy deviation). The regression analysis revealed that only 12 of them were statistically significant with the requirement that the standard deviation of each coefficient could not exceed 0.1 of the value of the respective coefficient.

The intensity distribution is then evaluated from data of about 2×10^9 particles. Such a calculation takes about 75 seconds. The initial conditions are generated according to the current density distributions of the virtual source. Fig. 3 shows an example of intensity profiles used in correction computation of a Ga^+ ion optical system. The plane of the sample is tilted under 45° and there is a positively biased detector, which acts in the direction of the x axis, causes a deflection and adds ellipticity to the spot shape. The dipole field extends approximately 2.5 mm from the sample center and its intensity is about 850 V/mm. The quadrupole field is roughly in the region from 0.5 mm to 2.5 mm from the sample and the average of its axial function p_2 is about 500 V/mm² [5].

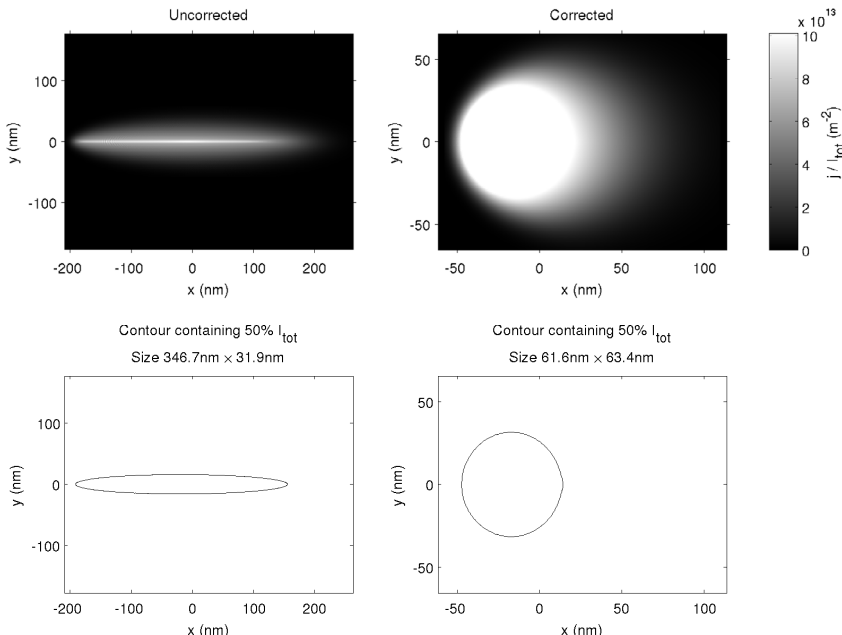


Fig. 3: Example of a correction achieved on a tilted sample in the presence of an extracting field of an analyzer (j and I_{tot} denote the current density distribution and the total beam current, respectively). The x axis is shifted by the deflection of the spot centers, 86 nm, caused by the extracting field. Virtual source parameters: size 5 nm (full width at half maximum, Gaussian distribution), aperture half-angle 0.57 mrad (uniform distribution), energy width 10 eV (FWHM, Gaussian distribution), primary beam energy: 25 keV. In this case the Gaussian image plane was located at the intersection of the tilted sample plane. The probe size can be further optimized by choosing a suitable defocus (moving the Gaussian image plane away from the sample plane).

References:

- [1] M. Oral, B. Lencová, Calculation of aberration coefficients by ray tracing, *Ultramicroscopy* **109** (2009), p. 1365-1373.
- [2] P. W. Hawkes, E. Kasper, *Principles of Electron Optics: Basic geometrical optics*, Volume 1, Academic Press (1994).
- [3] H. H. Rose, *Geometrical Charged-Particle Optics*, Springer-Verlag (2009) p. 93-111.
- [4] B. Lencová, J. Zlámal, A new program for the design of electron microscopes, *Physics Procedia* **1** (2008), p. 315-324
- [5] Acknowledgement: Supported by the Grant Agency of the ASCR, grant 100650805.

MAPPING THE LOCAL DENSITY OF STATES ABOVE VACUUM LEVEL BY VERY LOW ENERGY ELECTRON REFLECTIVITY

Z. Pokorná*, L. Frank

¹ Institute of Scientific Instruments v.v.i., Academy of Science of the Czech Republic,
Královopolská 147, 61264 Brno, Czech Republic

* e-mail: zuza@isibrno.cz

The local density of states is an important characteristic of solids, crystalline matters in particular. What used to be a pure theoreticians' toy is nowadays an experimentally accessible characteristic, e.g. by means of photoemission or scanning tunneling spectroscopy. Local density of states can reflect e.g. the local dopant concentration in semiconductors or discern between different crystal orientations, as each crystal face has a specific density of states. One way of probing the local density of states is to measure the reflectivity of very low energy electrons (units to tens of eV) from the sample surface. The reflectivity is principally inversely proportional to the local density of electronic states coupled to the impinging electron wave [1].

The influence of the density of electron states has been noticed already in the Very Low Energy Electron Diffraction (VLEED) field. The signal of the specularly reflected (0,0) diffraction spot below the threshold where the first nonspecular diffracted beam emerges is heavily modulated by the density of electron states above the vacuum level. Our experimental setup, a scanning electron microscope equipped by the cathode lens [2] (Fig. 1), is in fact an imaging version of the VLEED, allowing us to visualize the local energy dependence of the density of states across the sample at a high spatial resolution via mapping the reflectivity of the very low energy electrons. The cathode lens is a zero working distance electrostatic lens with the specimen serving as the cathode held at a tuneable negative potential, thus allowing one to decrease the energy of the incident electrons arbitrarily.

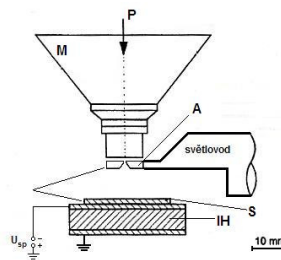


Fig. 1: Principle of the cathode lens in the Scanning Electron Microscope. P – primary beam, M – magnetic focusing lens, A – aperture of the scintillation detector (grounded, serving as anode of the cathode lens), S – specimen, IH – insulating holder.

Since differently oriented crystal faces have specific densities of states and therefore specific energy dependence of the very slow electron reflectivity is expected, a series of demonstration

experiments has been carried out on single crystal aluminum (111) and (100) specimens and on the high-grade highly ordered pyrolytic graphite. The reflectivity was compared to theoretical calculations [3,4] and the influence of surface cleanliness and other conditions was considered. The average brightness of each image was determined and plotted against energy. Since in the cathode lens at low energies a large portion of the signal escapes through the central scintillator bore, the collection efficiency drops. This effect was corrected by subtracting the sloping baseline.

The conclusion is that certain features of the electronic structure are indeed clearly visible in the very low energy electron reflectivity signal and well-defined or even in-situ prepared state of the specimen surface is of an utmost importance.

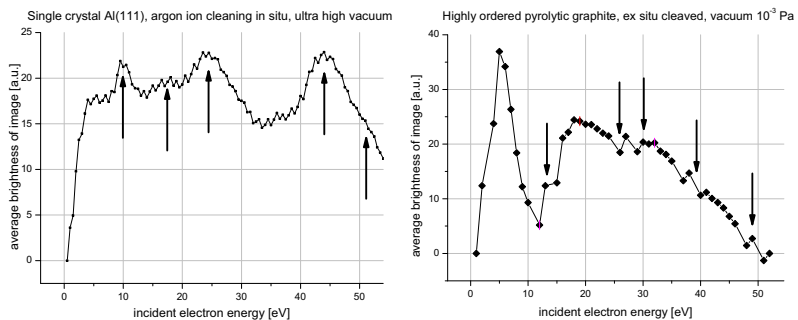


Fig. 2: Examples of the electron reflectivity spectra from single crystal specimens and from the highly ordered pyrolytic graphite with markers indicating pronounced features in the spectra.

References:

- [1] V. N. Strocov, H. I. Starnberg, Phys. Rev. B **52** (1995) 8759.
- [2] I. Müllerová, L. Frank, Adv. Imaging and Electron Phys. **128** (2003) 309.
- [3] E. Krasovskii, W. Schattke, Phys. Rev. B **56** (1997) 12874.
- [4] E. Krasovskii, Phys. Rev. B **70** (2004) 245322.

OPTIMIZATION OF THE COLLECTION EFFICIENCY OF SECONDARY IONS FOR SPATIALLY RESOLVED SIMS IN CROSSBEAM DEVICES

D. Preikszas^{1*}, M. Aliman¹, H. Mantz¹, A. Laue², A. Brockhaus² and A. Glasmachers²

¹ Carl Zeiss NTS GmbH, Carl-Zeiss-Straße 56, 73447 Oberkochen, Germany

² University of Wuppertal, Rainer-Gruenter-Straße 21, 42097 Wuppertal, Germany

* e-mail: preikszas@smt.zeiss.com

In a high-resolution Scanning Electron Microscope (SEM), equipped with a Focussed Ion Beam (FIB) in a Crossbeam configuration, the sample is located at the intersection point of the optic axes of the particle columns. Due to the limited space in front of the sample a Secondary Ion Mass Spectrometer (SIMS) can not be arranged close to it [1]. Therefore, adequate transfer optics is needed to extract and guide the secondary ions from the interaction region to the spectrometer.

Using high-frequency quadrupoles that are segmented and biased in axial direction and simultaneously cooling with Helium gas is an effective way for bunching the secondary ions and guiding them to the SIMS (figure 1). The cooling gas is confined to the housing of this quadrupole transfer optics (QTO), but at the inlet aperture it streams to the sample chamber. Since the necessary gas pressure in the cooling region is much higher than the maximum allowable vacuum pressure in the sample chamber, the resulting pressure difference has to be maintained by differential pumping. This pressure difference can only be reached with a very small inlet aperture of the QTO.

A small inlet aperture of the QTO however strongly reduces the solid angle of the emitted secondary ions that reach the SIMS. To increase the collection efficiency, an extraction voltage is applied to the QTO tip. In the hypothetical case that the QTO is arranged perpendicularly to the sample surface, an extraction voltage of -400V for example increases the collection efficiency for positive ions from about 0.4% to about 20% (see the focusing of the secondary ions in figure 2).

In practice, the FIB and not the QTO is arranged perpendicularly to the sample surface, and the objective lens of the SEM blocks a large portion of the available space. The QTO can only be implemented to the remaining space, resulting in the arrangement depicted in figure 3. In this arrangement the extraction field from the QTO tip is strongly distorted by the inclined sample and the objective lenses of FIB and SEM. Additionally, if the objective lens of the SEM consists of a detector lens that sucks secondary electrons of the sample to the lens by an electric field, even the leakage of this field influences the collection efficiency for the secondary ions. Without any countermeasures, the distorted electric extraction field forces most secondary ions to hit the QTO housing; nearly no ion enters the inlet aperture. However, using the tips of the objectives of FIB and SEM as independent electrodes, the shape of the electric extraction field can be varied, thus optimizing the collection efficiency for the SIMS.

For the specific example of a Crossbeam (Carl Zeiss NVision), the measurements show that the ion collection efficiency of the QTO inlet aperture is very poor if only an extraction voltage at this tip is used (yield less than 1% of the amount of produced secondary ions). If

appropriate potentials are applied to the tips of FIB and SEM, the collection efficiency is increased by at least a factor of 20. The maximum attainable efficiency depends on the tip potentials, the tip positions, and the tip shapes of FIB, SEM, and QTO.

The results also show that, for a given position of the QTO, it is always possible to obtain the best collection efficiency of the secondary ions regardless of the composition of the sample and the mass range. Additionally, the measurements illustrate that a highly accurate mechanical positioning of the QTO tip with respect to FIB and SEM is not required: The best collection efficiency for a given QTO tip potential can always be obtained only by choosing appropriate tip potentials at the FIB and SEM columns. Due to the optimized ion collection efficiency of the QTO both the scanning rate and the dynamic range of the spatially resolved SIMS analysis can be significantly increased. The presented method even works for both positive and negative ions by simply changing the polarity of the QTO tip and correspondingly adjusting the tip potentials of SEM and FIB.

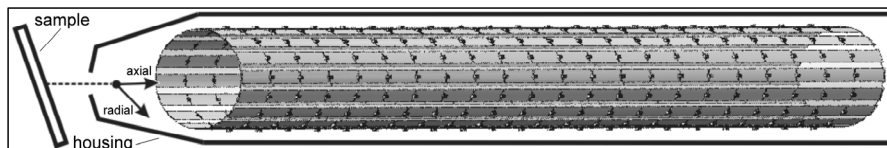


Figure 1: Arrangement of the quadrupole transfer optics (QTO) inside its housing.

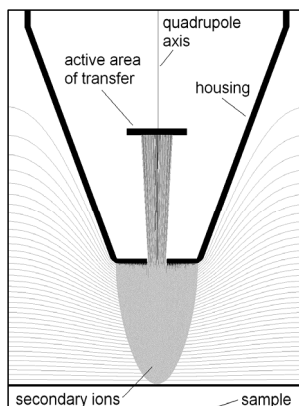


Figure 2: Tip of QTO with electric equipotentials.

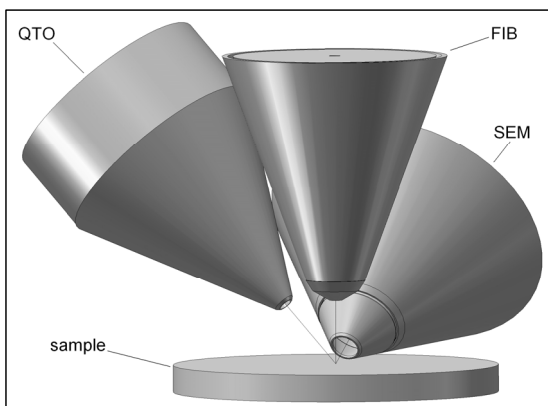


Figure 3: Arrangement of sample and tips of QTO, FIB, and SEM with intersecting axes.

Support by the BMBF (project 13N9430) is gratefully acknowledged.

References:

- [1] Aliman M. and Glasmachers A., JASMS **volume 10 no. 10** (1999), p. 1000-1007.

PROPERTIES OF Bi LMIS WITH ION CLUSTERS

T. Radlická¹

¹ Institute for Scientific instruments of the ASCR, v.v.i., Královopolská 147, Brno, Czech Republic

*e-mail: radlicka@isibrno.cz

The ion beams used in SIMS are produced by liquid–metal ion sources (LMIS) which provide fine, optically bright ion beams even for low emission currents around $1\mu\text{A}$ or less. The typical energy of the primary beam varies from 10 to 40keV. We study the function Bi LMIS whose use in SIMPS was described in [1,2]. The properties of the LMIS are strongly limited by the effect of the Discrete Coulomb Interactions (DCI) near the source. The DCI increase the energy width (Boersch effect) and decrease the brightness of the source due to the trajectory displacement effect. We have already studied these effects for a Ga LMIS at $1\mu\text{A}$ emission current [3]. Contrary to the Ga LMIS which contains mostly only Ga^+ ions [4], in case of the Bi LMIS the ion beam consists of several ion types and clusters of ions with similar currents, (Table 1). Because each ion type has different charge and mass they will be accelerated to different velocities, which increase the number of interactions and decreases the quality of the source. The aim of this contribution is a simulation of the effect of the clusters on the source properties based on the MC simulation.

Ion type	Bi^+	Bi2^+	Bi3^+	Bi3^{++}	Bi4^+	Bi5^+	Bi5^{++}	Bi7^+	Bi7^{++}
$I [\mu\text{A}]$	82.6	68.3	85.5	35.4	38.8	6.6	29.3	1.0	2.7

Table 1: Measured current of each cluster type on the sample in case of the emission current $0.2\mu\text{A}$ [5]. An aperture in front of the sample reduces the current to 0.17% of the emission current.

The initial conditions and emission time of all particles were set by MC methods. The partial beam currents determine the number of ions of each type and the time of the emission. The initial energy of ions was set according to the emission energy distribution [6] at temperature 545K. We assumed that the particles are emitted only from the spherical part of the Taylor cone perpendicularly to the surface. The radius of the source 0.54nm is determined by the evaporation field strength 18 V/nm [1], liquid density and surface tension.

The electrostatic potential in the system is the solution of the 2D Laplace equation in cylindrical coordinates. Because the ion gun length (about 20mm) is larger by seven orders of magnitude than the dimension of the Taylor cone diameter (less than 1nm), we calculate the global field and the local field near the source separately.

Raytracing is the most time-consuming part of the simulation. The motion of the particles is described by the equation of motion for particle beam in electrostatic field. It consists of part which represents the influence of the field of electrostatic lenses in the optical system and of the Coulomb sum - part describing particle-particle interactions in a beam. For the evaluation of the Coulomb sum we used the fast multipole method [7], which is an the $O(N)$ algorithm.

Moreover, the simulation in the vicinity of the tip, where the simulation time is mainly influenced by the strong field, and in the rest of the system, where the number of particles in the beam limits the calculation speed, were computed independently.

The increase of the energy width in the beam (Figure 1) is caused only due to the effect of DCI. The energy width is changing significantly just in the first micrometer from the tip. The figure also demonstrates different behavior for each ion type [8].

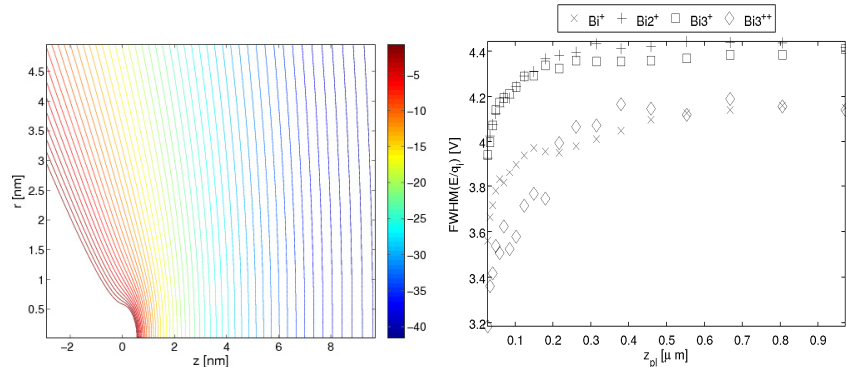


Fig. 1: The potential near the Taylor cone with the radius 0.54 nm and dependence of the width of the energy distribution of the beam on the axis on the distance from the tip for most important ions and clusters with charge q_i .

References

- [1] F. Kollmer, Cluster primary ion bombardment of organic materials, *Appl. Surf. Sci.* **231** (2004) 153-158.
- [2] F. M. Green et all, Imaging G-SIMS: a novel bismuth-manganese source emitter, *Rapid Com. Mass Spectrom.* **22** (2008) 2602-2608.
- [3] T. Radlička, B. Lencová, Coulomb interactions in Ga LMIS, *Ultramicroscopy* **108** (2008) 445-454.
- [4] R. G. Forbes and L. R. Mair, Liquid Metal Ion Source, in J. Orloff (ed.), *Handbook of charged particle optics*, CRC Press, 2009, 29-86.
- [5] F. Kollmer, private communication.
- [6] P. W. Hawkes, E. Kasper, *Principles of Electron Optics*, Academic Press, London, 1989.
- [7] H. Cheng, L. Greengard, V. Rokhlin, A fast adaptive multipole algorithm in three dimensions, *J. Comp. Phys.* **155** (1999) 468-498.
- [8] Acknowledgement: Work was supported by European Union under the grant number FP-7-200613 (3D Nanochemiscope).

ENERGY SELECTIVE SECONDARY ELECTRON DETECTION A SOLUTION TO SITE SPECIFIC SEM DOPANT MAPPING

C. Rodenburg^{1*}, M.A.E. Jepson², E.G.T. Bosch³, M. Dapor^{4,5}

¹ University of Sheffield, Dep. of Engineering Materials, Mappin Street, Sheffield, S13JD, UK

² Loughborough University, Department of Materials, LE11 3TU, Loughborough, UK

³ FEI Electron Optics, Achtseweg Noord 5, Acht, 5600 KA Eindhoven, The Netherlands

⁴ Centro Materiali e Microsistemi, FBK-IRST, via Sommarive 18, I-38123, Trento, Italy

⁵ Dipartimento di Ingegneria dei Materiali e Tecnologie Industriali, Università di Trento, via Mesiano 77, I-38123 Trento, Italy

*e-mail: c.rodenburg@shef.ac.uk

For decades secondary electron (SE) detection in most SEMs amounted to little more than counting the number of SEs to be translated into a gray scale image. This approach ignores information that is contained in the energy of the SE arriving at the detector in spite of the knowledge that SEs of different energies have different escape depths [1]. The latter implies that information can be gained if the energy range of SEs used for image formation can routinely be adjusted in SEMs. Such user defined energy selection can be performed in SEMs equipped with an Fei XL30 column, through adjusting the deflector voltage, D , see Fig 1. Here we demonstrate that energy selection in combination with some understanding of the surface of focused ion beam (FIB) prepared silicon specimens can be used to obtain dopant contrast as strong as that observed on freshly cleaved specimens (see Fig 2). This has not been possible to achieve without energy selection. The best possible dopant contrast achieved in standard SEM in the above column is less than 50% of that found on freshly cleaved specimens, and therefore insufficient to carry out site specific dopant mapping. Why energy selective dopant mapping enables site specific dopant mapping is explained below, based on Monte Carlo Modeling of the silicon and silicon oxide surface.

It is well known that Si surfaces exposed to Ga^+ in an FIB contain substantial amounts of implanted Ga and exhibit an electrically dead layer $\sim 25\text{nm}$ thick, when using Ga^+ energies $E_{\text{Ga}^+}=30\text{keV}$. These surfaces exhibit hardly any dopant contrast [2], because the majority of SEs escape from a distance, λ_{Si} , (mean escaped depth $\lambda_{\text{Si}}=7.5\text{nm}$ in Si [3]), a region located within the damaged layer. A reduction in ion energy leads to a reduced damage layer thickness. For example on an FIB section prepared by 10keV Ga^+ (damage thickness $\sim 10\text{nm}$ [4]), p-doped layers can be identified, however, in spite of the vastly different doping concentrations there is little variation in contrast (Fig 2). This is not surprising as λ_{Si} is still located within the damaged layer. The situation can be improved by increasing λ of the damaged layer by oxidizing it, through plasma cleaning (oxygen containing plasma) as $\lambda_{\text{SiO}_2}=16\text{nm}$ [5]. Hence for a 10keV FIB prepared surface a substantial number of SEs will escape from the material below the damaged layer. As these SEs contain dopant information, dopant contrast should be recovered. This is the case in Fig 2 where after plasma cleaning of the 10keV FIB prepared specimen the p-doped layers with different doping levels lead to different contrast, even in standard SEM.

However, the standard SEM contrast is still much less than that of a cleaved specimen. One reason is that n-and p-type silicon oxidize at different rates, with n-type oxidizing faster. This

will lead to a reduction in dopant contrast [6], because the SE yield for SiO_2 is larger than that for Si. As standard SEM only registers yield differences, the reduction in contrast as a consequence of oxidation is unavoidable, and offsets contrast gained by making the damaged layer transparent. This can be changed by using energy selection. As can be seen from the results of Monte Carlo simulations in Fig 3, the SE peak energy of SiO_2 covered Si is located above 5eV, the peak energy of Si well below 5eV. Selecting a ~3eV energy cut off allows the majority of SEs originating from the Si to reach the detector but prevents the detection of the majority of SEs that originated from the SiO_2 layer. Using this approach we can benefit from the enhanced dopant contrast by avoiding the damaged layer without losing this benefit as a result of the increase in SE yield of SiO_2 . The required energy selection for a 1keV incident electron beam is achieved by using a $D=16\text{V}$ at $T=250\text{V}$ and $WD=3\text{mm}$. This leads to a substantial increase in p-i-contrast compared to standard SEM and, for B-doping levels up to $9 \times 10^{18} \text{ cm}^{-3}$, to the same dopant contrast as observed in standard SEM as on freshly cleaved specimens. We expect that this can be achieved for all doping levels by using a filter with higher energy resolution or through refinement of the plasma oxidation procedure. If so, energy selective SEM could enable site specific SEM dopant mapping.

References:

- [1] M. P. Seah, W. A. Dench, *Surface and Interface Analysis* 1 (1) (1979) 2
- [2] P. Kazemian, A. C. Twitchett, C. J. Humphreys, C. Rodenburg, *APL* 88 (2006) 212110
- [3] K. Kanaya and H. Kawakatsu, *J. Phys. D: Appl. Phys.*, Vol. 5 (1972) 1727
- [4] Z. Wang et al., *Appl. Surf. Sci.* 241 (2005) 80
- [5] H.-J. Fitting, J. Boyde, J. Reinhardt, *physica status solidi (a)* 81 (1) (1983) 323
- [6] M. Dapor, M. A. E. Jepson, B. J. Inkson, C. Rodenburg, *Microsc. Microanal.* 15 (2009) 237

Fig. 1: ES system: positively biased extractor directs SEs to Deflector (3 layers of electrodes of opposite potential). The lowest layer deflects SEs to detector. Deflection field is adjusted by the deflector voltage, D .

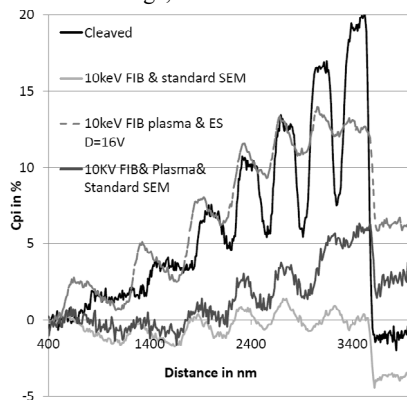


Fig. 2: Plots of the p-i-contrast, C_{pi} of a staircase structure with Boron doped layers from left to right: 4×10^{15} , 6.5×10^{16} , 8×10^{17} , 4×10^{18} , 9×10^{18} , 2×10^{19} cm^{-3} on As (10^{19} atoms cm^{-3}) doped Si.

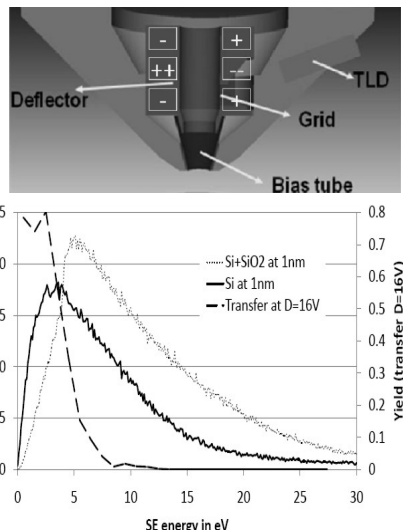


Fig. 3: SE spectra (obtained from Monte Carlo Modelling) for pure Si and Si covered with 2nm SiO_2 overlaid with detector transfer model for $D=16\text{V}$, $WD=3\text{mm}$, $T=250\text{V}$.

TRANSMISSION AND REFLECTION MICROSCOPY WITHOUT LENSES

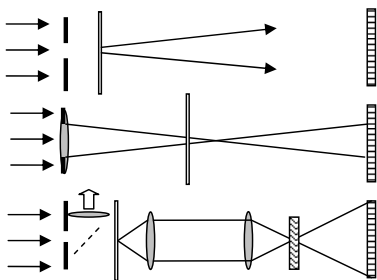
J. M. Rodenburg^{1*}, A. M. Maiden^{1,2} and M. J. Humphry²

¹ Dept. Electronic and Electrical Engineering, University of Sheffield, Mappin Street, S1 3JD, UK

² Phase Focus Ltd, The Kroto Innovation Centre, University of Sheffield, Broad Lane, Sheffield, S3 7HQ, UK

* e-mail: J.M.Rodenburg@shef.ac.uk

In this context, lensless imaging refers to the process of forming a transmission or reflection image by solving for the phase of a Fraunhofer or Fresnel diffraction pattern using a computational phase-retrieval algorithm. Pure diffractive imaging (Fig.1a), where only a roughly-localised incident beam impinges on the object and the scattered wavefield intensity is recorded in the far-field, can often more usefully be complemented by the use of poor



lenses to assist in the collection of diffraction patterns. Fig. 1b shows a configuration relevant to electron microscopy: the lens is used to localise the beam on the object. Other configurations (Fig.1c) include the use of a downstream lens to map the size of the diffraction pattern to the detector, or to form an image where a phase plate or aperture re-scatters the radiation (this increases the signal scattered to high angle, where high-resolution information

Figure 1: (a) top, (b) middle and (c) bottom. See text for details.

resides), the beam then being left to propagate to the detector. Reflection images can be created by the use of a beam-splitter, the detector optics then being positioned perpendicular to the incident beam.

We do not have space here to review the very many computational algorithms that have been developed over the last thirty years to solve for the phase of a diffraction pattern from its intensity alone. Suffice it to say that a recent innovation – ptychographical iterative methods – is vastly more efficient and mathematically well-conditioned than earlier algorithms. The method relies on illuminating the object at a number of different positions [1]. To cope with the fact that the illuminating beam itself can be complex-valued and soft-edged, a weighting factor [2] allows for the use of any form of structured illuminating beam. In fact, the illumination function itself can also be determined by variants of this approach. So, to make a microscope, all we need is a coarse optic of some sort (perhaps just an aperture) and a detector. See Figure 2 for examples.

There are many advantages of this roundabout means of imaging. For visible light, working distances can be very large (centimetres) without compromising resolution, the absolute phase information recovered has very high contrast (eg for imaging of live, unstained cells), and

focusing of the image can occur after the experiment is complete. For electron and X-ray microscopy, the very limited numerical apertures (and hence resolution) available with current lens technology can be surpassed.

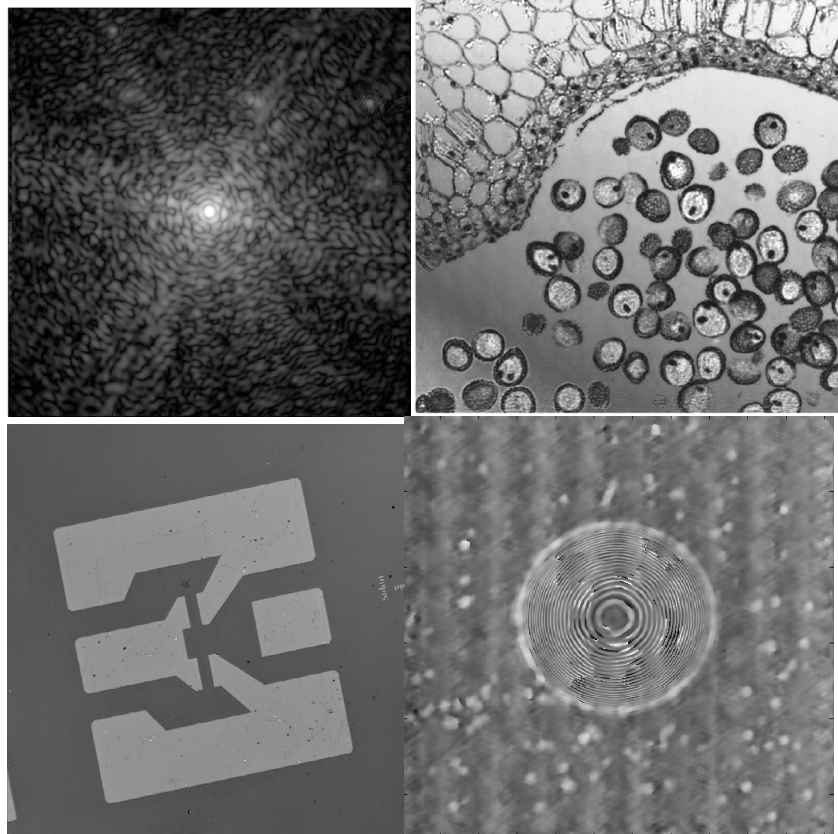


Figure 2: Clockwise for top right: a typical visible-light diffraction pattern; a lensless reconstruction of lily pollen, field of view approximately 700 μm ; the phase of an X-ray reconstruction of a gold test specimen, field of view 50 μm [3]; the phase of the reflection reconstruction of a semiconductor device.

References:

- [1] Faulkner H. M. L. and Rodenburg J. M, Phys. Rev. Lett. **93** (2004), No. 023903
- [2] Rodenburg J. M. and Faulkner H. M. L Appl.Phys.Lett (2004) **85** 4795
- [3] Rodenburg, J. M., Hurst, A. C., Cullis, A. G., Dobson, B. R., Pfeiffer, F., Bunk, O., David, C., Jefimovs, K. and Johnson, I, Phys. Rev. Lett. **93**. . (2007) No. 034801.

OUTLINE OF AN ABERRATION-CORRECTED LOW-VOLTAGE PHASE ELECTRON MICROSCOPE

H. Rose

Institute of Applied Physics, Technical University Darmstadt
Hochschulstrasse 6, 64287 Darmstadt, Germany
e-mail: harald.rose@physik.tu-darmstadt.de

The optimum operation mode of aberration-corrected electron microscopes depends strongly on the material of the object and on the properties to be investigated. To avoid atom displacement, the accelerating voltage must be lower than the knock-on threshold which lies in the range between 20 and 80kV for low-Z material. In order to achieve atomic resolution and to obtain a large field of view at such low acceleration voltages, we must correct for the chromatic aberration, the spherical aberration and the off-axial coma of the imaging system. Such a system forms an achromatic electron-optical aplanat. We employ electric and magnetic quadrupoles for the chromatic correction and octopoles for eliminating the spherical aberration.

To avoid off-axial aberrations, the corrector arrangement and the path of the Gaussian rays must be highly symmetric, as shown schematically in Fig. 1. This achroplanator consists of a telescopic round-lens transfer doublet and two telescopic multipole quintuplets [1]. They allow one to excite crossed electric and magnetic quadrupole fields compensating for the chromatic aberration and octopole fields for eliminating spherical aberration and coma. The corrector utilizes the symmetry principles of the hexapole corrector [2], which can only compensate for the spherical aberration of the objective lens. To enable correction of chromatic and spherical aberration, each of the two hexapole elements is replaced by a symmetric telescopic multipole quintuplet.

To enhance the contrast of weak phase objects, we propose an adjustable obstruction-free electrostatic phase shifter, acts like the Zernike phase plate utilized in light microscopy. The proposed phase shifter changes the phase of the scattered wave by an adjustable value for spatial frequencies q within a large range $q_{\min} \leq q \leq q_{\max}$, $q_{\max}/q_{\min} \geq 100$. In order to avoid obstruction by the field-forming electrodes, it is advantageous to perform the phase shift at anamorphotic images of the diffraction plane [3]. We obtain such strongly first-order distorted stigmatic images by the quadrupole system shown in Fig. 2. The quadrupoles form stigmatic images which are enlarged in one direction and compressed in the orthogonal direction. These line-shaped images enable us to shift the phase of the scattered wave without any obstruction by means of micro phase plates depicted in Fig. 3.

References

- [1] H. Rose, Geometrical Charged-Particle Optics, Springer, Heidelberg, 2009.
- [2] H. Rose, Outline of a spherically corrected semi-aplanatic medium-voltage TEM, Optik 85 (1990) 19-24.
- [3] R. Schroeder, B. Barton, B., H. Rose, G. Benner, Contrast enhancement by anamorphotic phase plates in an aberration-corrected TEM, Microscopy and Microanalysis 13, Suppl. 3 (2007) 008-009.

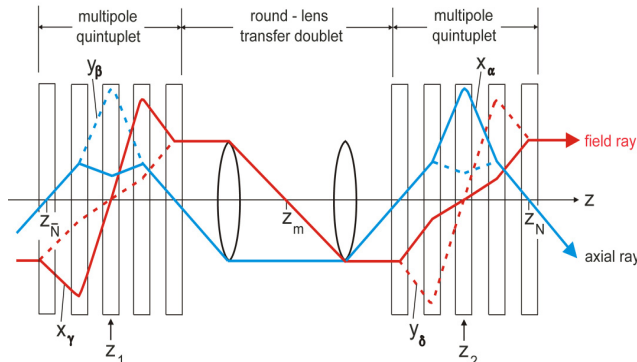


Fig. 1: Schematic set-up of the achroplanator, anamorphotic images of the diffraction plane are formed at the centers z_1 and z_2 of each telescopic multipole quintuplet

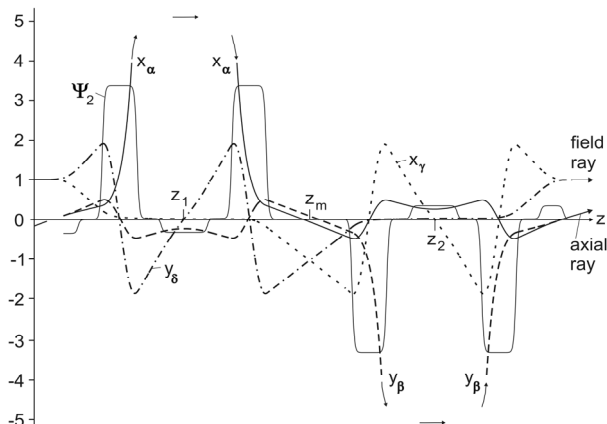


Fig. 2: Course $\Psi_2 = \Psi_2(z)$ of the axial magnetic quadrupole strength and course of the field rays x_α, y_δ and the axial rays x_α, y_β , respectively, along the optic axis within the phase shifter. Anamorphotic images of the diffraction plane are located at the planes z_1 and z_2 where the phase plates are placed.

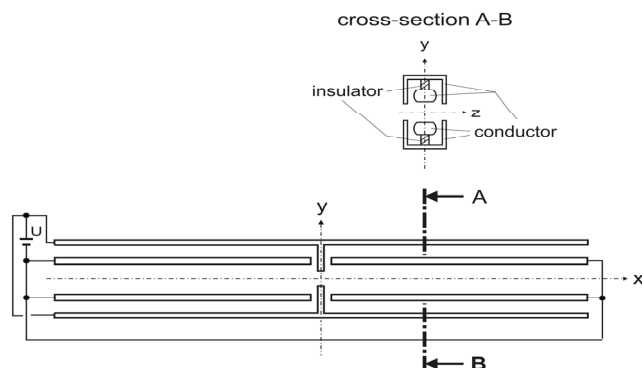


Fig. 3: Scheme of the obstruction-free phase plate, U is the voltage between the outer and inner conductors

NANOSTRUCTURE AND MORPHOLOGY OF WOOD CARBON OBSERVED BY LOW VOLTAGE ELECTRON MICROSCOPY

K. Sato^{1*}, T. J. Konno¹, K. Suzuki² and T. Suzuki²

¹ Institute for Materials Research, Tohoku University, Sendai, Japan

² Department of Biotechnology & Environmental Chemistry, Kitami Institute of Technology, Kitami, Japan

*e-mail: ksato@imr.tohoku.ac.jp

Wood carbon, known as carbon neutral material, is a promising candidate for a future energy resource. The nanostructure and morphology of the wood carbon are sensitive to the fabrication process, such as wood species, metal catalyst, and/or annealing temperatures. In this study we employed low voltage electron microscopy to visualize nanostructure of wood carbon prepared by iron-, nickel-, or cobalt-catalyzed carbonization and subsequent oxidation processes [1-4].

Topographical morphology was observed by a Hitachi SU8000 or an S-5500 scanning electron microscope (SEM) operating at 1.5-30 kV with a field emission gun (FEG). Structure of wood carbon was characterized by an FEI Titan 80-300 transmission electron microscope (TEM) operating at 80kV with an FEG and a CEOS aberration corrector for the objective lens.

SEM observation revealed that the length of graphite shell chains (GSCs) formed from hardwood is shorter than those from softwood. It is also noticed that GSCs formed from softwood tend to exist on the surface area of carbides, while those formed from hardwood were not found on the surface area. These results suggest differences in a formation mechanism of GSCs between softwood and hardwood. Figures 1(a) and (b) compare secondary electron (SE) images of softwood observed at 30 kV and 1.5 kV, respectively, after carbonization at 900°C with 2%Fe catalyst. Surface morphology of GSCs can be imaged clearly by using low energy electrons. In contrast, details inside GSCs are imaged by transmission mode (bright-field STEM) at 30 kV as shown in Fig.1(c). High magnification SEM images are shown in Fig.2. The SE image is sensitive to the surface topography of GSCs while the BF-STEM image can reveal the inside.

Shell structures of graphitic carbon and lattice fringes were observed in the wood carbon prepared at 900°C followed by oxidation at 480°C after removal of the metal catalyst particles. Well-defined crystal lattice was observed in the case of softwood, while hardwood showed degradation of the graphite lattice. Figures 3(a) and (b) show TEM images of typical GSCs for softwood carbonized with 2%Fe catalyst. In addition to the hollow GSCs, dark contrast region was also observed as shown by arrowheads in Fig.3(c). Based on EDS elemental analyses, these dark contrast were found to be residual Fe catalyst nanoparticles. Annular dark-field STEM images as well as back scattered electron (BSE) images also indicated the distribution of Fe nanoparticles.

This study was partially supported by the Center for Integrated Nanotechnology Support at Tohoku University and also by “Nanotechnology Network Project” of the Ministry of Education, Culture, Sports, Science and Technology, Japan. The authors wish to thank Mr. E. Aoyagi and Mr. Y. Hayasaka for their help using SEM and TEM.

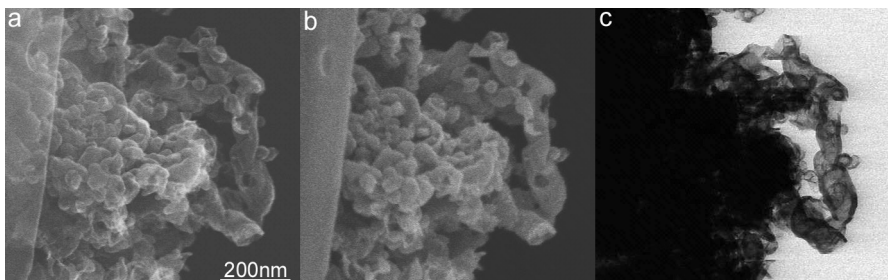


Figure 1: SEM images of softwood carbonized with 2%Fe catalyst (S-5500). (a) SE image at 30 kV, (b) SE image at 1.5 kV, and (c) BF-STEM image at 30 kV.

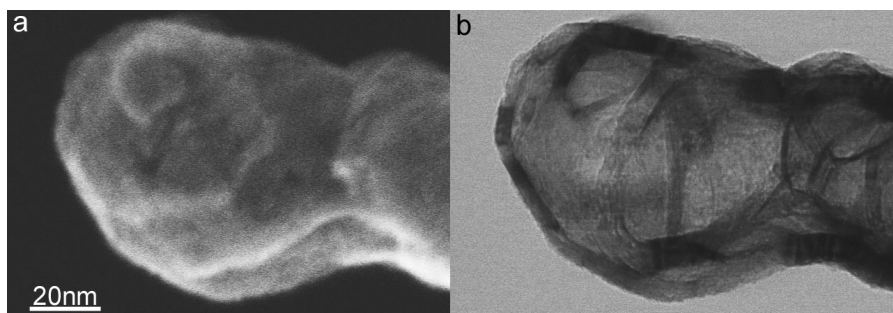


Figure 2: High magnification SEM images of softwood carbonized with 2%Fe catalyst (S-5500). (a) SE image at 30 kV, and (b) BF-STEM image at 30 kV.

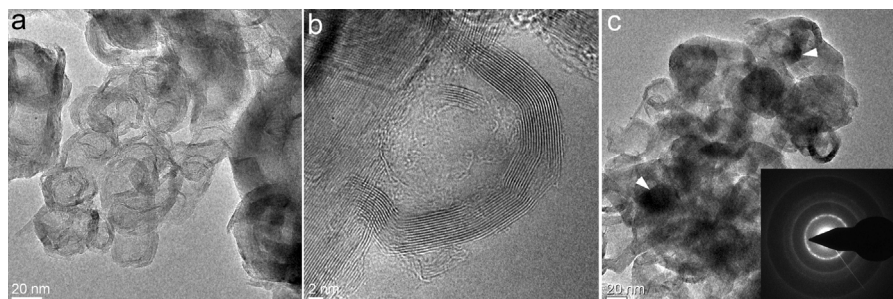


Figure 3: C_s -corrected TEM images (80 kV) of typical GSCs for softwood carbonized with 2%Fe catalyst. Hollow GSCs with graphitic carbon structure are seen.

References:

- [1] K. Suzuki, T. Suzuki, Y. Takahashi et al. Chem. Lett., **34** (2005) 870-871.
- [2] T. Suzuki, K. Suzuki, Y. Takahashi et al. J. Wood Sci. **53** (2007) 54-60.
- [3] T. Suzuki, H. Matsuzaki, K. Suzuki et al. Chem. Lett., **37** (2008) 798-799.
- [4] K. Suzuki, T. Suzuki, Y. Takahashi et al. J. Wood Sci., **55** (2009) 60-68.

DETERMINATION OF PROXIMITY EFFECT FORWARD SCATTERING RANGE PARAMETER IN E-BEAM LITHOGRAPHY

M. Urbánek, V. Kolařík, S. Král and M. Dvořáková

Institute of Scientific Instruments AS CR, v.v.i., Královopolská 147, 612 64, Brno, CR

* e-mail: urbanek@isibrno.cz

Electron beam lithography (EBL) is a tool for generation patterns with high resolution, so it is necessary to control critical dimensions of created patterns, because the undesired influence of adjacent regions to those exposed can occur due to the proximity effect. Proximity effect is often described by two Gaussian function, where α represents forward scattering range parameter [1,3]. Consequently, we present evaluation of proximity parameter α [1,2] by various method in this paper.

A test pattern for EBL exposure were designed as following [3]: test pattern consists of alternating lines and gaps formation, ambient line (changing width of line from 0,5 µm to 5 µm with step 0,5 µm), gap of width = 0,5 µm, central line of width = 0,5 µm, gap of width = 0,5 µm and ambient line (changing width of line from 0,5 µm to 5 µm with step 0,5 µm, see fig.1). The intensity slope γ of deposited energy at the edge of the central line relates to parameter α according to $\gamma = -2/\sqrt{\pi}\alpha$ [3], therefore it is necessary to measure width of central line. Each pattern was exposed for relative dose from 20 % to 110%.

A testing exposure was carried out on E-beam writer system TESLA BS600 using acceleration voltage of 15 kV and rectangularly shaped beam (stamp size 0,5 µm * 0,5 µm). The exposure dose corresponding to a reference (100%) dose was 5 µC/cm². As a resist we used FEP-171 of thickness = 180 nm spun on Si wafer. Prior to exposure the FEP-171 was baked for 120 s at 124 °C. Post Exposure Baking (PEB) was done for 110 s at 123°C after exposure. After PEB, TMAH developer was used for 25 s at 23 °C in the developing process.

It is necessary to characterize central lines width of designed patterns for determination forward scattering range parameter. The exposed patterns were characterized by several methods (optical microscopy, confocal microscopy, scanning electron microscopy (fig.2) and atomic force microscopy). The goal was to compare reliability of different methods and to find the most suitable one for characterization of designed test pattern for proximity parameter determination. From the graph (figure 3) it is obvious that the results from various methods are almost identical and methods provide reliable data. Nevertheless the optical microscopy method is the most time consuming and scanning electron microscopy requires metal coating of surface, which can distort dimensions of testing pattern. The theoretical value of the forward scattering range parameter for given resist thickness $d_f = 0,9(R_t/V_b)^{1/5}$ [4] is much less than measured values, because influence of material is not considered.

More detailed study is necessary in order to find backscattering range parameter and understand proximity effect completely.

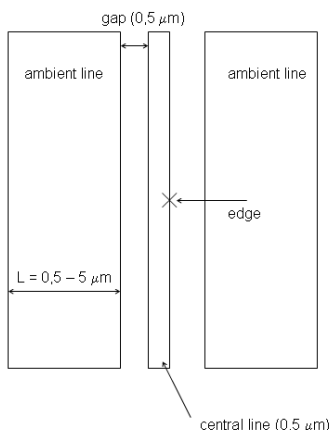


Figure 1: Scheme of testing pattern (according to [3]).

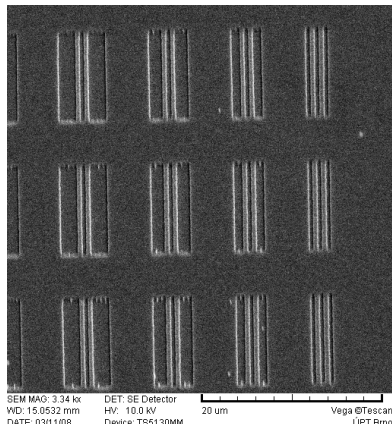


Figure 2: SEM micrograph of testing pattern (TESCAN VEGA TS 5130MM, magnification 3,34 k).

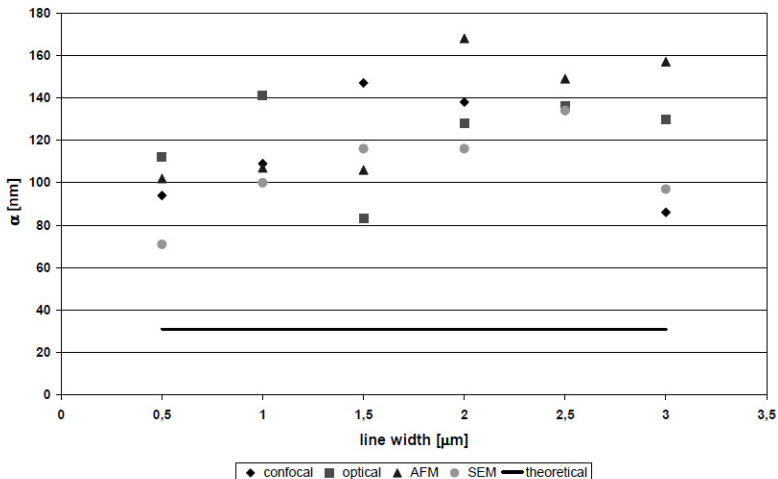


Figure 3: Parameter α for various method of characterization.

References:

- [1] G. Owen, Journal of Vacuum Science Technology B, **8(6)**, (1990), 1889-1892.
- [2] A. van de Kraats, <http://nanolithography.gatech.edu/proximity.htm>.
- [3] E. Seo, B.K. Choi, O. Kim, Microelectronic Engineering, **53** (2000), 305-308.
- [4] P. Rai-Choudhury, Handbook of microlithography, micromachining and microfabrication, volume 1: microlithography.

This work was partially supported by MIT CR under the contract No. FR TI1/576 and by EC and MEYS CR (project No. CZ.1.05/2.1.00/01.0017 ALISI).

IMAGING OF THERMAL TREATED THIN FILMS ON SILICON SUBSTRATE IN THE SCANNING LOW ENERGY ELECTRON MICROSCOPE

J. Zobačová^{1*}, Š. Mikmeková¹, J. Polčák² and L. Frank¹

¹ Institute of Scientific Instruments of the ASCR, v.v.i., Královopolská 147, 612 64, Brno, Czech Republic

² Institute of Physical Engineering, Brno University of Technology, Technická 2896/2, 616 69, Brno, Czech Republic

*e-mail: zobacova@isibrno.cz

Structure of thin films usually requires to be examined on microscopic level. The research topics like growth and stability of thin films, phase transitions and separation, crystallization, diffusion and defect formation has a need for LEED or XPS as techniques adequate for investigation of atomic transport processes on short length scales. The low energy electron microscopy is a complementary solution for imaging of samples with special concern for knowledge of surface physics and material science.

In this contribution the microscopic examination of as-deposited and thermal treated thin films on Si substrates is performed. The poly-crystalline copper film of 450 nm in thickness was sputter deposited on Si substrates at TU Clausthal. The samples were annealed at 150 °C for 3 minutes, respective at 630 °C for 30 minutes. Both samples were taken out of the vacuum chamber half an hour after termination of the heating process. The SEM Vega TS 5130MM with standard vacuum conditions, equipped with the cathode lens (CL) [1], was used to examine the structural changes of samples caused by the thermal treatment – see the micrographs of the as-deposited and annealed samples in Fig. 2 and 3.

In Fig. 1 we notice the secondary electron (SE) and backscattered electron (BSE) micrographs of the as-deposited Cu film with an average grain size in units of μm . The SE image was acquired with the standard Everhart-Thornley type of detector collecting a portion of SE emitted at higher polar angles with respect to the surface normal and at azimuthal angles oriented toward the detector. The BSE micrograph is contributed by SE accelerated within the CL field and partly escaping detection through the CL bore (mainly those at lowest energies), and by BSE collimated toward the detector by the CL field so that higher polar angles are acquired [1]. Obviously the grain contrast is much higher in the BSE micrograph and even some twinning boundaries can be observed. The CL mode enables us to record the BSE images at arbitrary low landing energies of electrons and is capable of collecting even BSE emitted close the zero take-off angle.

In Fig. 2 we compare the as-deposited Cu film and the same heated at 150 °C. In the heated sample somewhat enlarged grains are apparent together with dots of the high temperature (HT) oxide. In Fig. 3 we notice growth of the copper oxide islands owing to annealing at 630 °C. In the centre of the field of view we see a grain with suppressed creation of the HT oxide, however with a structure the appearance of which modifies throughout the energy scale. While at high energy of electrons some patchy coating or contamination can be believed, at medium energy a structure is more clearly visible of small “grains” similar to those in Fig. 1, however with widened and rounded boundaries and much reduced planar contrast between them. At low energy we see an undulating surface relief of a similar typical dimension. Likely explanation is that we observe the low temperature native oxide the thickness of which reflects “footprints” of the original structure of small grains via dependence of the oxidation rate on the crystal orientation and the grain boundary conditions. Variations in appearance of

the structure with electron energy are connected with changes in the penetration depth, ratio between SE and BSE contributions and angular acceptance of the detector.

Electrons backscattered under large angles from the optical axis are not available for detection in conventional devices and also low and very low energy BSE are traditionally abandoned. The CL mode offers significant extension to the BSE imaging in the SEM, providing considerably enhanced crystallinic information. [2]

References:

- [1] Müllerová I. and Frank L., *Adv. Imaging & Electron Phys.* **128** (2003), p. 309-443.
- [2] Study supported by the Grant Agency of ASCR under no. IAA 10065080.

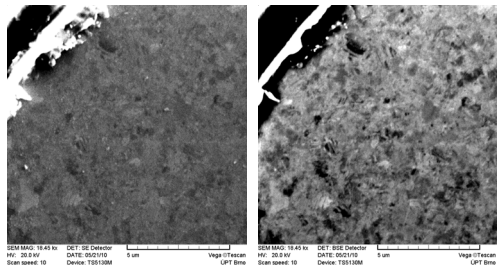


Fig. 1: The as-deposited Cu film: SE image at 20 keV (left) and BSE image at 18 keV taken in the CL mode with primary energy of 20 keV (right).

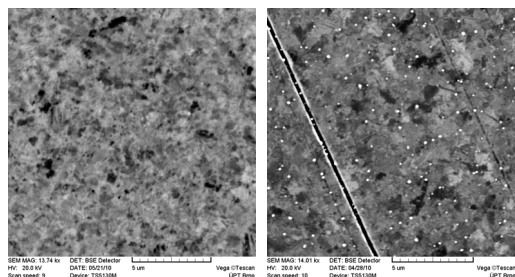


Fig. 2: The BSE images of the as-deposited specimen (left) and the same annealed at 150 °C for 3 min; CL mode, landing energy 15 keV, primary energy 20 keV.

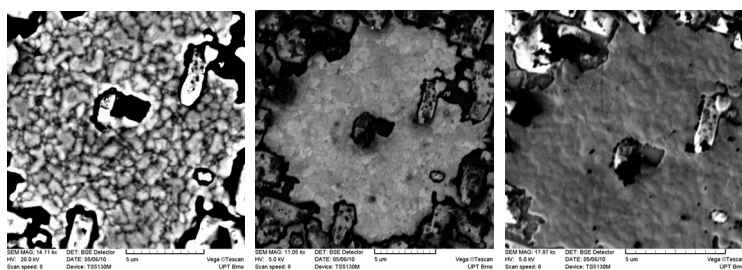


Fig. 3: The BSE image of a certain area on the specimen annealed at 630 °C for 30 min; landing/primary energy was 15/20 keV (left), 3.75/5 keV (middle), and 0.5/5 keV (right).

